Connection between the Asian Summer Monsoon and the Middle Latitudes through the Geopotential Height Anomaly over the Western Tibetan Plateau

Takeshi Watanabe

Division of Environmental Science Development,

Graduate School of Environmental Science,

Hokkaido University

February 2013

Abstract

This study aims to develop a better understanding of the relationship between the intraseasonal variations of the Asian summer monsoon and variation at higher latitudes and focuses on the variation of geopotential height over the western Tibetan Plateau in May and June (early summer).

The geopotential height index (hereafter called as the “GPH index”) is defined as area-averaged geopotential anomaly at 200 hPa over the western Tibetan plateau where large intraseasonal variability of geopotential height is observed in early summer. The composite concerning the marked positive GPH index shows the anticyclonic anomaly over the western Tibetan plateau, which is most developed at day 0, is related to the wave-propagation from the northern Atlantic Ocean and the wave train along the subtropical jet propagates eastward after day 0. The wave-like anomaly from the Arabian Sea to Southeast Asia at 850 hPa appears after day 0 and retains for a week. Applying the Rossby ray-path theory it is found the low-level westerly from the Arabian Sea to the Southeast Asia acts as a Rossby wave guide. It is suggested that the wave-like anomaly observed at 850 hPa is the quasi-stationary Rossby wave.

The mechanism of relation between the middle latitudes and the Asian monsoon in early summer is explained briefly as follows: The anticyclonic anomaly over the western Tibetan plateau develops the heat-low over the northwestern South Asia. The anomalous westerly wind over the Arabia Sea is strengthened due to the heat-low and interacts with the topographic barrier over the Indian subcontinent. The anticyclonic anomaly is generated. Then low-level Rossby wave propagates eastward along the low-level westerly. The negative composite shows similar distribution with the positive composite, but the sign is opposite.

Precipitation over South and Southeast Asia increases/decreases for a week after the anticyclonic/cyclonic anomaly over the western Tibetan plateau develops, respectively, because of the low-level Rossby wave. At the same time the positive/negative anomaly of near-surface temperature persists, which is caused by the clear/clouded sky and decreasing/increasing of precipitation. However, before the development of the upper-level anticyclonic anomaly precipitation over South and Southeast Asia increases because the anomaly with the wave-number 1, which is like the Madden-Julian Oscillation, appears and makes convection over the northern Indian Ocean active.

The marked wave-train which propagates from the north Atlantic to the western Tibetan plateau can be traced back to the northeastern North America. At the same time the MJO-like disturbance is observed in the tropics. The OLR anomaly shows active convection over the northern Indian Ocean and suppressed convection over Central America. Results of numerical experiments using a linear baroclinic model show that convection over both Central America and the northern Indian Ocean generates the anticyclonic anomaly over the western Tibetan plateau constructively. It is suggested that the western Tibetan Plateau is the region where the effects in the tropics and middle latitudes tend to be concentrated, and it is thought to be an important connection between the Asian monsoon and middle latitudes.

Contents

1. General introduction

1.1. Introduction

The monsoon is defined as the annual reversal of low-level winds originally and characterized by contrast of rainy and dry seasons. Several regional monsoons are recognized on the globe. Zhang and Wang (2008) proposed the strong regional monsoons defined by using two criteria; the annual reversal of low-level winds and contrast of rainy and dry seasons. The Asian monsoon is the largest and most outstanding of all the regional monsoons.

The Asian monsoon shows considerable variability at various time scales from climatological to diurnal scales. Heavy and large impacts of variation of the Asian monsoon on the human society in Asia, such as. natural disaster and water resources, motivate researchers to work on scientific problems of the Asian monsoon.

This study is concerned with the intraseasonal variation of the Asian summer monsoon. This intraseasonal variation is influenced by disturbances both in the tropics and in the higher latitudes;. The Madden-Julian Oscillation (MJO) is one of the most important sources from the tropics (Madden and Julian 1994; Kemball-Cook and Wang 2001; Pai et al. 2011). As the active convective part of the MJO arrives in the Indian Ocean and moves eastwards into the Maritime continent, precipitation in South and Southeast Asia tends to increase (Pai et al. 2011). Kemball-Cook and Wang (2001) investigated boreal summer intraseasonal variation during two separate periods (May–June and August–October) because of the pronounced differences in their climatologies. In both periods, convection over the Indian Ocean propagates along the equator and then moves poleward. This poleward shift of convection is caused by Rossby waves emitted by the equatorial convection. Convection in May–June shows continuous propagation along the Maritime continent, while convection in August–October transfers from the Indian Ocean to the western Pacific.

Previous studies have shown the relationship between the Asian monsoon and anomalies in the middle

latitudes and subtropics, and indicate that the wave train at higher latitudes is connected to the variation of the Asian summer monsoon (Fujinami and Yasunari 2004; Wang et al. 2008; Ding and Wang 2009; Krishnan et al. 2009). These studies also found a marked anomaly over Central Asia and the western Tibetan Plateau. Ding and Wang (2009) showed that a Rossby wave train across the Eurasian continent, and the summer monsoon convection in the northwestern India and Pakistan, are coupled at an intraseasonal time scale, and hypothesized a positive feedback between the Eurasian wave train and Indian summer monsoon. The intraseasonal variability of geopotential height over Central Asia and the western Tibetan Plateau is large in early summer (Fig. 1.3; discussed in detail in section 1.2). The above studies emphasized the influence of the middle latitudes upon the tropical monsoon. However, tropical convection also affects the mid-latitude atmospheric circulation. For instance, convection in the South and Southeast Asian monsoons influences the vertical motion over Southwest and Central Asia in the subtropics (Rodwell and Hoskins 1995; Zhang et al. 2004). This suggests that the anomaly extending from Central Asia to the western Tibetan Plateau is an important connection point in the relationship between the subtropics and the Asian summer monsoon.

Based on numerical experiments Wang et al. (2008) suggested that enhanced diabatic heating on the Tibetan plateau is responsible for the excitation of Rossby waves that propagate along the subtropical jet; additionally, their Fig. 3 shows wave propagation in the lower level, although this aspect was not discussed in detail in their paper. The low-level Rossby wave is thought to be one of mechanisms of connection between the Asian summer monsoon and the middle latitude.

1.2. Overview of the climatology over the Asian monsoon region in early summer

The present section describes the overview of the climatology over Asia. The data used in the present section is The 6-hourly reanalysis data, provided by the European Centre for Medium-Range Weather Forecasts (ECMWF) (ERA40; Uppala et al. 2005), which is described in detail later in Section 1.4.

Figure 1.1 shows climatologies of zonal wind speed at 200 hPa and 850 hPa in a period from 1958 to 2002 averaged between 60° and 110°E. The Asian subtropical jet is located around 30°N at the first of May and migrates northward between May and June (Fig. 1.1a). The Asian subtropical jet arrives at 40°N and situated there between July and August. The low-level westerly from Arabian Sea to Southeast Asia holds up during summer monsoon season (Fig. 1.1b). The strength and distribution of these westerlies vary with the activity of the South Asian monsoon (Joseph and Sijikumar 2004). The low-level westerly starts to develop from May, accelerates rapidly at the onset of South Asian summer monsoon and then dominates the South and Southeast Asian monsoon regions until October (Webster et al. 1998). The westerly is strongest between June and July. Early summer, between May and June, represents the transition season for the Asian summer monsoon (Zhang and Wang 2008). The basic condition of the atmosphere over Asia changes considerably with the seasonal change during the summer monsoon season. Consequently, for the purposes of research into the intraseasonal variability of the Asian summer monsoon, the summer monsoon season must be divided into distinct periods.

Figure 1.2 shows climatologies of zonal wind speed at 200 hPa and 850 hPa for a period in early summer from May to June. The Asian subtropical jet is around 35°N (Fig. 1.2a). The low-level westerly is from Arabian Sea to Southeast Asia along 15°N (Fig. 1.2b).

Figure 1.3 shows the intraseasonal variability of the geopotential height at 200 hPa in May and June. The intraseasonal variability was calculated as the root-mean-square of the anomaly from the daily climatology from 1948 to 2002, from which each year's average was removed; i.e., the intraseasonal variability shown in Fig. 1.3 does not include the interannual variability. A large intraseasonal variability is seen over the western Tibetan Plateau in May and June, at which time the Asian subtropical jet is located around 35°N (Fig. 1.2a).

Figure 1.4 shows the first eigenvector for the intraseasonal variability of geopotential height at 200 hPa in a period from May to June (Fig, 1.4). The eigenvector was obtained from the principal component analysis by applying the generalized spatial weighting matrix that was introduced by Baldwin et al. (2009). The first eigenvector has its center of variation over the western Tibetan Plateau, and a wave-like distribution along the subtropical jet.

Fig. 1.5 shows the lag-correlation map between the principal component for the first eigenvector and geopotential height at 200 hPa. Geopotential height is backward or forward against the principal component. The variation of geopotential relative to the dominant variation around the Tibetan plateau shows that the wave-train propagates from the northern Atlantic Ocean to the western Tibetan plateau and that the distribution shown by the first eigenvector corresponds to the eastward propagating wave train along the subtropical jet.

1.3. Outline of the present study

This study aims to develop a better understanding of the relationship between the intraseasonal variations of the Asian summer monsoon and variation at higher latitudes. Considering the results of previous studies and characteristics of climatologies in summer monsoon season we focus on the variation of geopotential height over the western Tibetan Plateau in May and June (early summer).

Three subjects are selected along the purpose and are worked on in three chapters one by one. The outline of the present study is as follows: Chapter 2 describes the relation between the middle latitudes and the Asian monsoon in early summer. Chapter 3 describes the variation of weather over the Asian monsoon region related to the variation of geopotential height over the western Tibetan plateau. Chapter 4 describes the causes of the marked variation of geopotential height over the western Tibetan plateau. Results of the present study are summarized in Chapter 5.

1.4. Data

Reanalysis data set, outgoing longwave radiation (OLR) and precipitation data are used in this thesis.

1) The 6-hourly reanalysis data, provided by the European Centre for Medium-Range Weather Forecasts (ECMWF) (ERA40; Uppala et al. 2005) on a 2.5° × 2.5° grid, were used for May and June between 1958 and 2002. The analyzed variables were zonal and meridional wind velocities, temperature, and

geopotential height. Stream function and velocity potential were calculated by using the expansion into the spherical harmonics function with truncation of T25. Daily averaged data were used to remove the influence of diurnal variability.

2) The daily averaged outgoing longwave radiation (OLR) data, provided by the National Oceanic and Atmospheric Administration/Climatic Diagnosis Centers (NOAA/CDC) on a 2.5° × 2.5° grid, were available over the period from 1975 to 2002 (Liebmann and Smith 1996).

3) rain-gauge-based data, in the form of the 0.5° gridded daily precipitation product developed by the Asian Precipitation Highly Resolved Observational Data Integration Towards Evaluation of water resources (APHRODITE) project (Yatagai et al. 2009), were available for monsoon Asia (60°–150°E, 0°–55°N) between 1961 and 2002.

The daily climatology was calculated by averaging the data for each day over the period of each dataset, and then smoothing these data using a 5-day running mean. The anomaly was defined as the deviations from this daily climatology.

1.5. Linear baroclinic model

The dry linear baroclinic model (hereafter called as the "LBM"), which was constructed based on a linearized AGCM (atmospheric general circulation model) developed at the former Center for Climate System Research (CCSR), the University of Tokyo, and the National Institute for Environmental Studies (NIES) (Watanabe and Kimoto 2000). The selected horizontal and vertical resolutions were T42 and 11 levels, respectively. The damping time scale was set at 1 day for the lowest and topmost levels, and 20 days for the other levels. The dry LBM doesn't include the process of diabatic heating such as condensation heating and radiation.

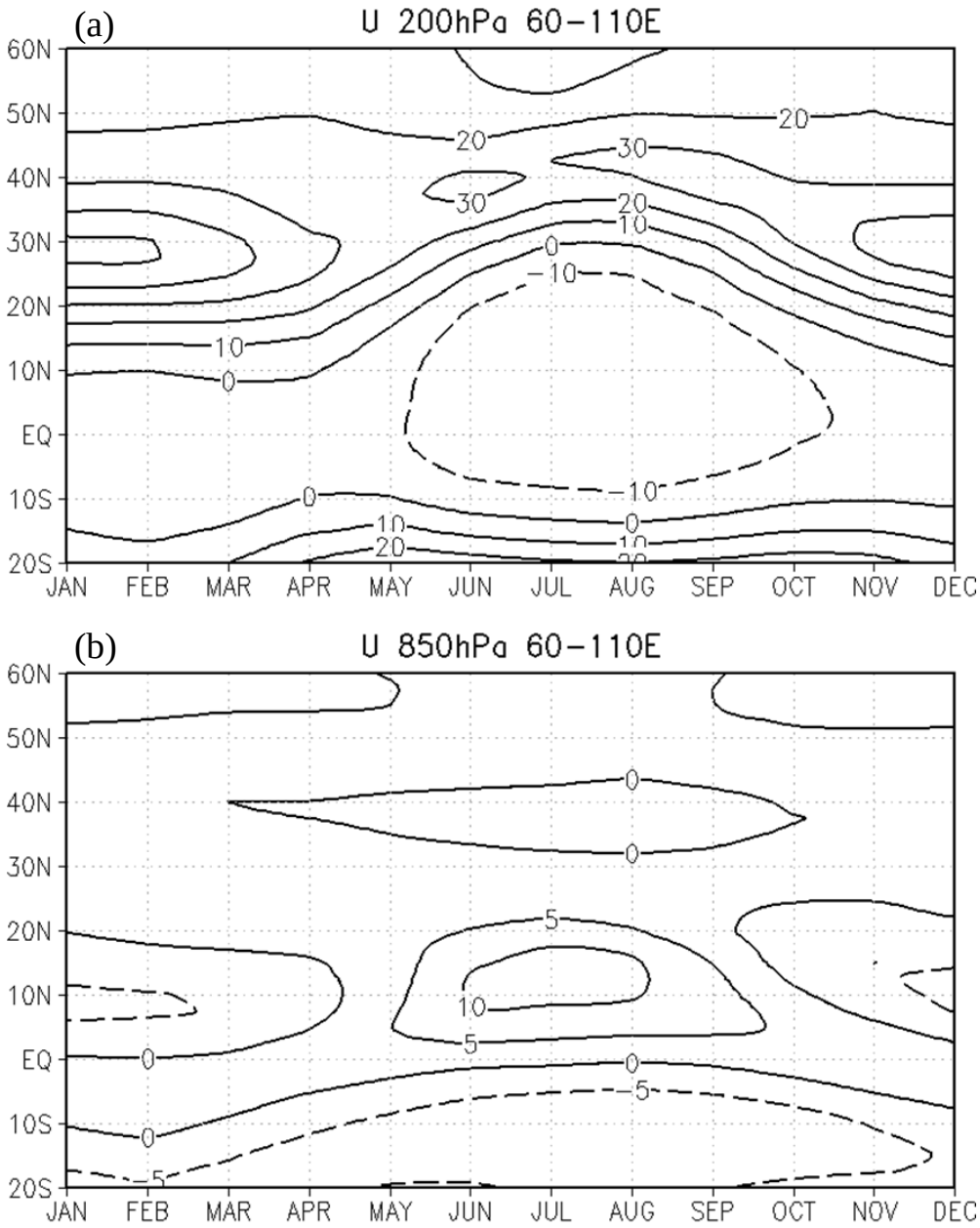

Fig. 1.1. Climatologies of zonal wind speed at (a) 200 and (b) 850 hPa averaged between 60° and 110°E. The contour interval is 10 m s^{-1} in (a) and 5 m s^{-1} in (b).

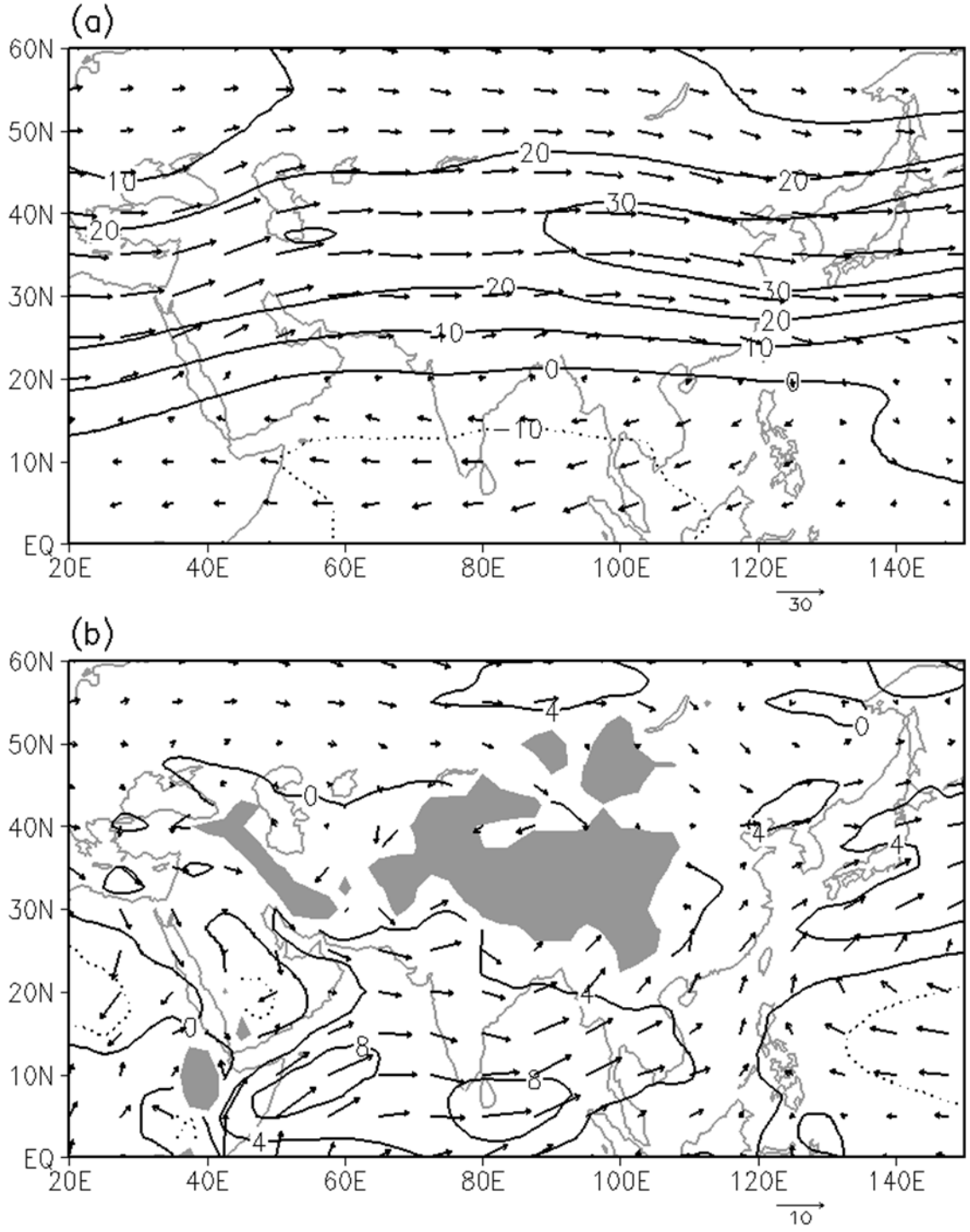

Fig. 1.2. Climatologies of horizontal wind (vector) and zonal wind speed (contour) in a period from May to June at (a) 200 and (b) 850 hPa. The contour interval is 10 m s^{-1} in (a) and 4 m s^{-1} in (b). Gray shaded areas in (b) represent topography above 1500 m.

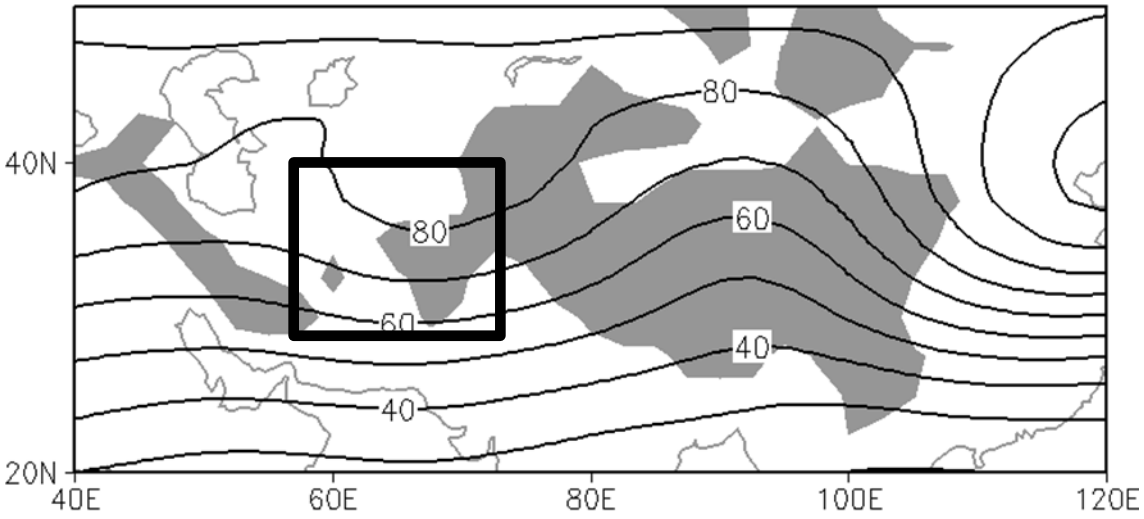

Fig. 1.3. Intraseasonal variability of geopotential height at 200 hPa in May and June. Contour interval is 10 m. Gray shaded areas represent topography above 1500 m. The rectangle represents the region where the GHP index is defined.

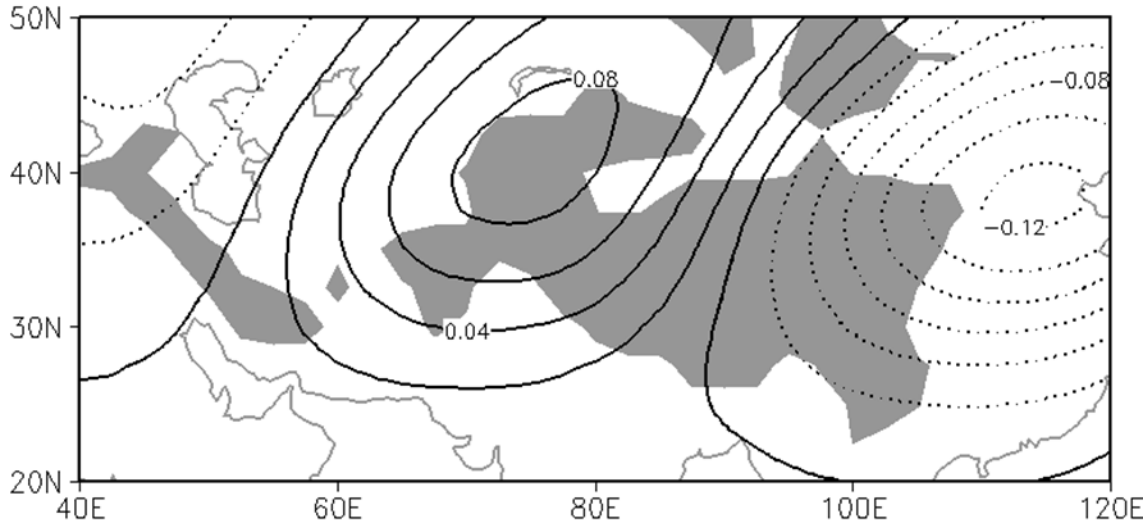

Fig. 1.4. The first eigenvector of intraseasonal variance of geopotential height at 200 hPa in May and June. The eigenvector is non-dimensional.

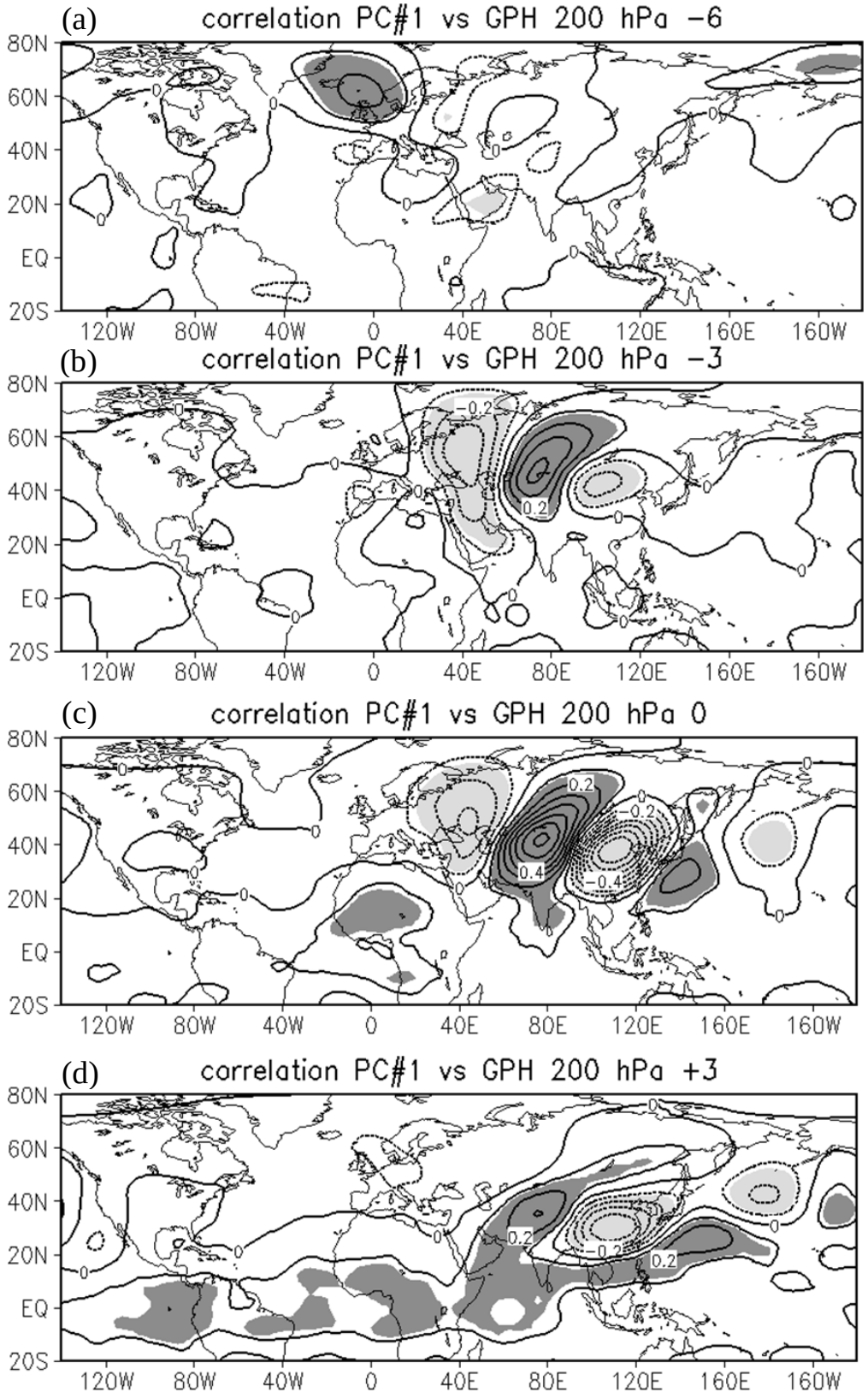

Fig. 1.5. Lag-correlaion between the principal component of the first eigenvector shown in Fig. 1.4 and geopotential height at 200 hPa. Geopotential height is behind (a) 6 days, (b) 3 days and (c) 0 days, and (d) forward 3 days against the principal component. Contour interval is 0.1.

2. Relation between the subtropics and the Asian monsoon in early summer

2.1. Definition of the GPH index

As shown in Chapter 1 the intraseasonal variability of geopotential height at 200 hPa over the western Tibetan plateau is remarkable in early summer. Then the geopotential height index (hereafter called as the "GPH index") is defined as the anomaly of geopotential height averaged over the western Tibetan plateau (30°–40°N, 60°–75°E; see a rectangle in Fig. 1.3). A positive GPH index indicates an upper-level anticyclonic disturbance over the western Tibetan plateau. The GPH index is standardized with its standard deviation.

2.2. Method

The main technique employed in this chapter is composite analysis. Firstly the key day of positive/negative composite is defined as the day when the standardized GPH index is more/less than +1.5/–1.5 respectively and is selected for the interval of each key day to be more than 20 days. If there are some key days in 20 days the larger one is chosen. This procedure was repeated until all the key days were separated by more than 20 days.

Then key days of positive/negative composite are selected 35/40 over a period of 45 years, respectively (Table 1 and 2). Some years have more than one key day and some have no key day. However, the long-term trend and interdecadal variation of the frequency of key days are not identified. The composite with respect to the key days of a variable is called day 0, and the time series of composites is computed for the 10 days either side of the key day. The composite of X days before/after the key day is referred to as day +/- X

2.3. Result of the composite analysis

Figure 2.1 shows the composite for geopotential height at 200 hPa. Also shown is the wave activity computed from the composite for the stream function and the climatology in May and June (Takaya and Nakamura 2001). The wave train propagates from the northern Atlantic Ocean to the western Tibetan plateau via the western Russia from day -7 to day 0 (Fig. 2.1a-h). Each center of geopotential height anomaly along propagation path attend a maximum at day -7 over the northern Atlantic Ocean (Fig. 2.1a), at day -2 over the western Russia (Fig. 2.1f) and at day 0 over the western Tibetan plateau (Fig. 2.1h). After day 0 the wave train propagates from the western Tibetan plateau along the subtropical jet. The anticyclonic anomaly over the western Tibetan plateau is declined (Fig. 2.1i).

Figure 2.2 shows the composite for horizontal wind at 850 hPa. The anomalous westerly appears from the Arabian Sea to the Bay of Bengal at day 0 (Fig. 2.2a). After day 0 the wave-like anomaly from Arabian Sea to the Bay of Bengal appears and retained for about a week (Fig. 2.2b-d). The anticyclonic anomaly over the Indian subcontinent is developed only at low-level while the cyclonic anomaly over the Bay of Bengal reaches about 400 hPa (Fig. 2.3). The cyclonic anomaly over the northern Arabian Sea develops rapidly after day 0 (Fig. 2.2b and 2.2c). The anomalous wind accompanied by the cyclonic anomaly blows toward the Indian subcontinent and the south side of the western Tibetan plateau.

The result of composite shows the intraseasonal variation of geopotential height over the western Tibetan plateau is related to the variation of circulation in South and Southeast Asia.

2.4. Low-level Rossby wave

Figure 2.4 shows a longitude–time diagram of anomalous vorticity along 15°N at 850 hPa. The alternating generation of anticyclonic and cyclonic anomalies is seen to propagate eastward over time. The anomalous vortices extend eastward from the southeast of the Arabian Sea/Indian subcontinent at 70°E (day +2) to the

Bay of Bengal at 85°E (day +4) and the Indochina Peninsula at 105°E (day +6). The wave-like anomalies are quasi-stationary and each vortex is maintained for about 4 days. The bold line with an arrow head in Fig. 2.4 represents the propagation path of the low-level wave train. The average propagation speed (group velocity) is 10° per day (about 12 m s^{-1}). The average wavelength is about 3700 km and then the zonal wavenumber is about 10. Assuming that the zonal wave number is equal to the meridional wave number the total wave number is estimated as 14.

The Rossby ray-path theory (Hoskins and Ambrizzi 1993) is applied to the region with strong low-level westerly. According to the theory, the stationary wavenumber K is defined as follows:

$$K = \left(\frac{\beta_*}{\overline{U}} \right)^{1/2}, \qquad (2.1)$$

where

$$\beta_* = \beta - \frac{\partial^2 \overline{U}}{\partial y^2} \qquad (2.2)$$

is the meridional gradient of absolute vorticity, $\overline{U}$ is zonal wind speed and β is .the planetary vorticity gradient.

A strong westerly belt, in which the absolute vorticity shows strong meridional variability, acts as a Rossby waveguide (Hoskins and Ambrizzi 1993). The waveguide has a unique distribution of stationary Rossby wavenumber, whereby a zonal belt of higher total wavenumber is sandwiched by zonal belts of lower total wavenumber. The Rossby wave propagates eastward in the Rossby waveguide, refracted toward latitudes with a higher wavenumber.

Figure 2.5a shows the composite of the raw zonal wind at 850 hPa at day +4. Strong westerlies, exceeding 8 m s^{-1}, occur over the Arabian Sea and the Bay of Bengal between 5° and 20°N. The path of the wave-like anomaly follows this strong westerly belt. Figure 2.5b shows the total stationary wavenumber, K, calculated from the raw zonal wind in Figure 2.5a by using eq. (2.1). The distribution of the zonal belt with a high total wavenumber along 15°N is sandwiched by zonal belts with a low total wavenumber, which is typical for a waveguide. The wave number of the trapped stationary Rossby wave in the waveguide is from 11 to 16, which corresponds well to the observed wavenumber. It appears that the strong westerly belt acts as a waveguide and

that the low-level anomaly propagates eastward along the waveguide in the form of a quasi-stationary Rossby wave.

2.5. Mechanisms that explain the influence of the upper-level anomaly on the lower-level anomaly

With the initial propagation of the lower-level anomaly, the westerly wind over the Arabian Sea, accompanied by the cyclonic anomaly centered at the Thar Desert and neighboring arid regions (hereafter called as the "TD regions"), is strengthened (Fig. 2.2 and 2.6). The findings of Gadgil (1977) indicate that this strong anomalous southwesterly is likely to cause the anticyclonic anomaly over the Indian subcontinent through its interaction with topography; i.e., the Western Ghats, which are oriented north–south and have an average elevation of 1200 m. The situation for a westerly flow impinging on a topographic barrier is shown in figure 4.9 of Holton (2004). In this figure, the anticyclonic flow pattern appears to the east side of the mountain barrier, followed by an alternating series of ridges and troughs downstream. This pattern arises because the vertical extent of air columns in the westerly decreases over the mountain barrier, resulting in reduced relative vorticity. Thus, the air columns acquire an anticyclonic vorticity. The Western Ghats is likely to act as the barrier, interacting with the columns in the southwesterly flow. To conserve the absolute vorticity, an anticyclonic anomaly appears over the Indian subcontinent, followed by the start of eastward propagation of the lower-level anomaly in the waveguide. Thus, the development of the cyclonic anomaly over the TD region is considered to cause the subsequent eastward propagation of the lower-level Rossby wave. The remainder of this section examines how the lower-level cyclonic anomaly over the TD region is associated with the upper-level anticyclonic anomaly.

Figure 2.7 shows a time–pressure diagram for the composite of anomalous geopotential height averaged over the TD region. Until day –1, an increase in anomalous geopotential is seen at all levels. In the upper and middle levels, anomalous geopotential height increases until day 0, whereas it starts decreasing in the

lower-level after day –1 and the negative geopotential height anomaly shows rapid development. The negative geopotential height anomaly attains a maximum in the lowest level at day +2, two days after the maximum anticyclonic anomaly in the upper level at day 0, corresponding to the appearance of a cyclonic anomaly over the TD region (see Fig. 2.2b). The development of the low is evident in the composite for surface pressure (Fig. 2.6).

Figure 2.8 shows latitude–pressure cross-sections along 70°E for composites of anomalous meridional and vertical wind vectors and anomalous temperature at day 0 and day +2. This region contains the center of the upper-level anticyclonic anomaly and the lower-level cyclonic anomaly. At day 0, strong anomalous descent is evident over mountain ranges of Hindu Kush and the Karakoram (hereafter called as "H–K mountain ranges") between 30°N and 40°N (Fig. 2.8a). To the south, anomalous descent is observed between the middle and lower levels, along the slopes of the H–K mountain ranges. These anomalous descents appear at day –4 and are strengthened with the development of the upper-level anticyclonic anomaly. The vertical distribution of anomalous circulation shows a marked change from day 0 to day +2. At day +2, the pronounced anomalous descent over the H–K mountain ranges disappears (Fig. 2.8b). Anomalous ascents are generated in the upper level to the north and south of the H–K mountain range, but thereafter show a rapid decline.

At day 0, a higher-temperature anomaly is located over the H–K mountain ranges in the upper level (Fig. 2.8a). The higher-temperature anomaly between the middle and lower levels, which is vertically almost uniform, corresponds to anomalous descent (Fig. 2.8a). Therefore, adiabatic heating, strengthened by anomalous descent, causes an increase in temperature at the middle and lower levels. Composite for temperature at a height of 2 m shows the developed positive anomaly more than 2 K is below the upper-level anticyclonic anomaly and is retained (Fig. 2.9).

Given the topographic and atmospheric conditions, it is supposed that the development of the anomalous low over the TD region is similar to that of a heat-low (Blake et al. 1983; Smith 1986), which can be observed in a shallow layer at the bottom of the deeply developed mixed layer over desert areas. Blake et al. (1983) and Smith (1986) demonstrated that the heat-low over the Saudi Arabian Desert is generated from adiabatic heating

associated with strong subsidence at all levels, solar heating in the lower level, and near-surface sensible heating.

To identify the origin of the change in vertical motion, the Q-vector is used to diagnose the vertical motion. The Q-vector form of omega equation is written as

$$\sigma\nabla^2\omega + {f_0}^2\frac{\partial^2\omega}{\partial p^2} = -2\nabla\cdot\vec{Q} + f_0\beta\frac{\partial v_g}{\partial p} - \frac{\kappa}{p}\nabla^2 J \ , \qquad (2.3)$$

where

$$\vec{Q} = (Q_1, Q_2) = \left(-\frac{R}{p}\frac{\partial\overrightarrow{V_g}}{\partial x}\cdot\nabla T, -\frac{R}{p}\frac{\partial\overrightarrow{V_g}}{\partial y}\cdot\nabla T\right) . \qquad (2.4)$$

The Q-vector diagnoses vertical motion due to adiabatic flow in the ω-equation, under quasi-geostrophic theory (Hoskins et al. 1978), and can be computed from temperature and height fields. The divergence/convergence of the Q-vector indicates dynamically forced descent/ascent by a geostrophic motion.

Figure 2.10 shows composites for the anomalous vertical p-velocity and the Q-vector at 400 hPa at day 0. Mid-latitude regions show a good correspondence between divergence/convergence of the Q-vector and the positive/negative vertical p-velocity. The anomalous descent (ascent) to the east (west) of the anticyclonic anomaly corresponds to divergence (convergence) of the Q-vector. A similar correspondence is also seen down to 700 hPa (not shown). Therefore, the anomalous descent along 70°E is generated by the anticyclonic anomaly directly and adiabatically.

To investigate the response of the low-level circulation to the heating from the low-level to surface over the TD region a numerical experiments based on the LBM was carried out. In the experiment, an elliptic heat source, with a zonal 15° radius and meridional 10° radius of +3 K/day was placed over the TD region (centered at 65°E, 35°N), with its maximum at around 850 hPa, and was sustained for the integration period. The result shows the low-level wave train from South Asia to Southeast Asia (Fig. 2.11).

Lastly results of the negative composites are shown in Fig. 2.12. The negative composite for upper and low level circulations show the similar results with the positive composite, but the sign is reverse (Figs. 2.1h and 2.2b).

2.6. Summary

In the present chapter the relation between the middle latitudes and the Asian monsoon in early summer is investigated. The major analysis method in the present chapter is composite analysis. The GPH index is defined as the geopotential height anomaly averaged over the western Tibetan plateau at 200 hPa. Composites are calculated concerning marked positive and negative GPH index. The major results are summarized below.

1) Results of composite analysis concerning the marked positive GPH index shows the anticyclonic anomaly over the western Tibetan plateau is related to the variation of circulations between South and Southeast Asia. The anomaly of geopotential height at 200 hPa attends a maximum at day 0. The wave-like anomaly from the Arabian Sea to Southeast Asia at 850 hPa appears after day 0 and is retained for about a week. The negative composite shows similar distribution with the positive composite, but the sign is reverse.

2) Applying the Rossby ray-path theory it is found the low-level westerly from the Arabian Sea to the Southeast Asia acts as a Rossby wave guide which traps the Rossby waves with wavenumber from 11 to 16. The propagating path and wavenumber of the observed wave-like anomaly are consistent with theoretical results. The wave-like anomaly at 850 hPa from the Arabian Sea to the Southeast Asia is suggested to be the trapped Rossby wave.

3) The mechanism of relation between the middle latitudes and the Asian monsoon in early summer is summarized as follows:

   (1) The upper-level anomalous anticyclone over the western Tibetan plateau promotes the development of a heat low over the TD region, through adiabatic heating associated with strong subsidence and near-surface sensible heating. The strong subsidence is generated by the upper-level anticyclonic

anomaly dynamically. At the same time the cloudless weather is retained under the upper-level anticyclonic anomaly so that temperature near surface becomes high due to sensible heating.

(2) The anomalous southwesterly over the Arabian Sea associated with the heat-low blows toward the western Indian subcontinent, where it interacts with the topographic barrier over the Indian subcontinent. Then the anticyclonic vorticity is generated.

(3) The low-level Rossby wave propagates eastward along the westerly belt which acts as the Rossby wave guide. The quasi-stationary anomaly is retained for about a week.

Table 1. List of key days for positive composite.

3	June	1959	1	May	1959	17	May	1960	3	June	1961	9	May	1961
2	June	1963	16	June	1966	5	May	1966	9	June	1967	28	May	1969
18	May	1970	26	June	1970	9	June	1971	13	June	1973	17	June	1975
6	June	1978	22	June	1980	2	May	1981	7	June	1982	14	June	1984
5	May	1986	6	June	1987	14	May	1990	22	June	1990	15	June	1991
10	June	1993	20	June	1994	13	May	1995	22	June	1996	16	May	1998
28	June	1998	9	May	1999	8	May	2000	12	May	2001	11	May	2002

Table 2. List of key days for negative composite.

29	May	1958	5	May	1960	29	June	1962	30	June	1963	7	June	1964
11	May	1966	24	May	1967	14	June	1967	7	May	1968	13	May	1969
22	June	1969	6	June	1972	24	June	1974	4	May	1975	9	June	1975
19	June	1976	31	May	1979	14	June	1981	30	June	1982	14	May	1982
14	May	1985	4	June	1986	21	June	1987	7	May	1987	5	June	1988
2	May	1989	21	June	1989	25	June	1991	28	May	1991	4	May	1992
29	May	1992	10	May	1993	25	June	1993	25	May	1995	22	June	1995
14	May	1996	17	May	1997	11	June	1997	14	June	1998	24	June	1999

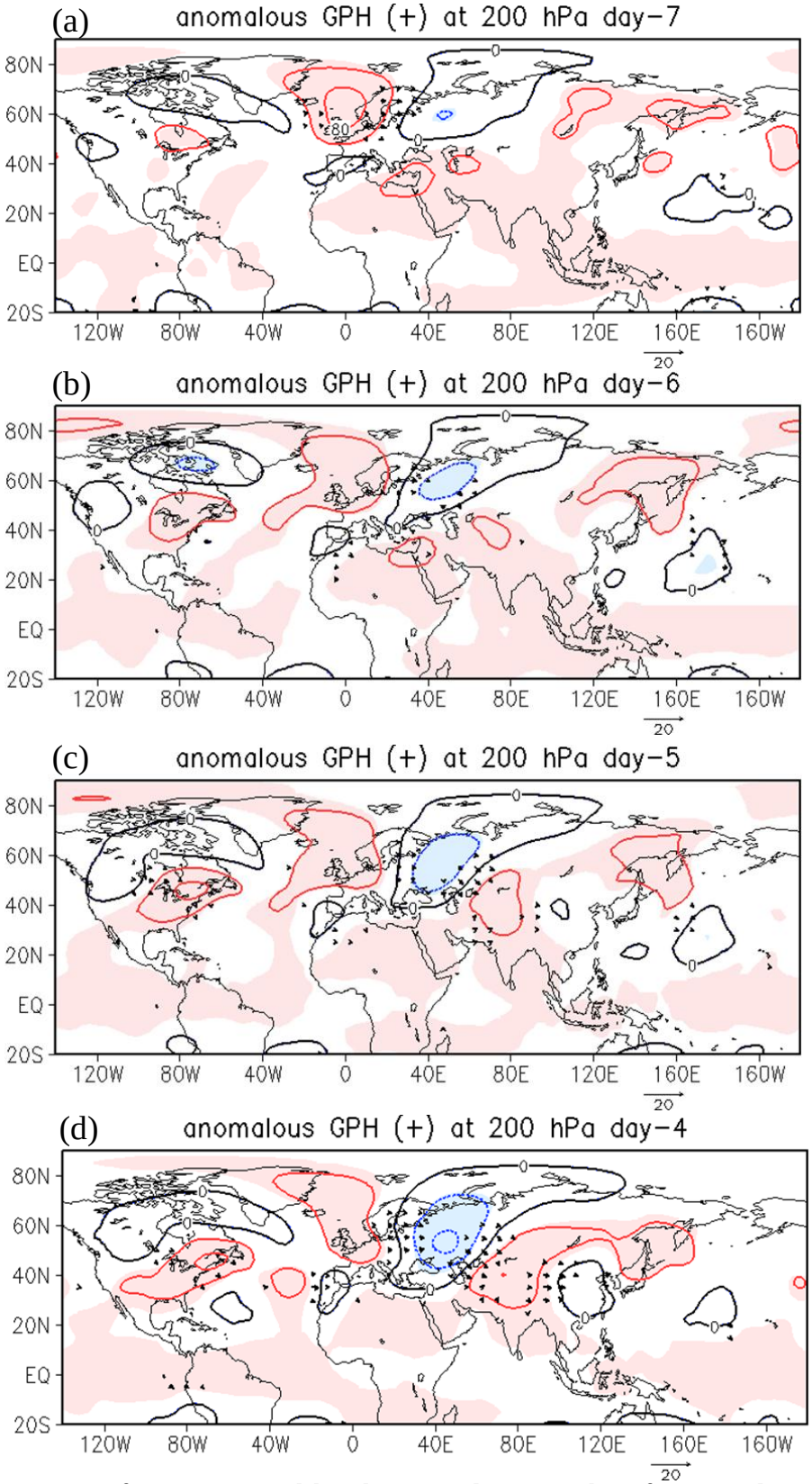

Fig. 2.1. Composites for geopotential height anomaly at 200 hPa from (a) day-7 to (l) day +4. Contour interval is 40 m. Shade represents statistically 95% confidence level. Arrows represent the wave activity flux, and are plotted at grid points where the magnitude of wave activity flux is greater than 1 $m^2 s^{-2}$.

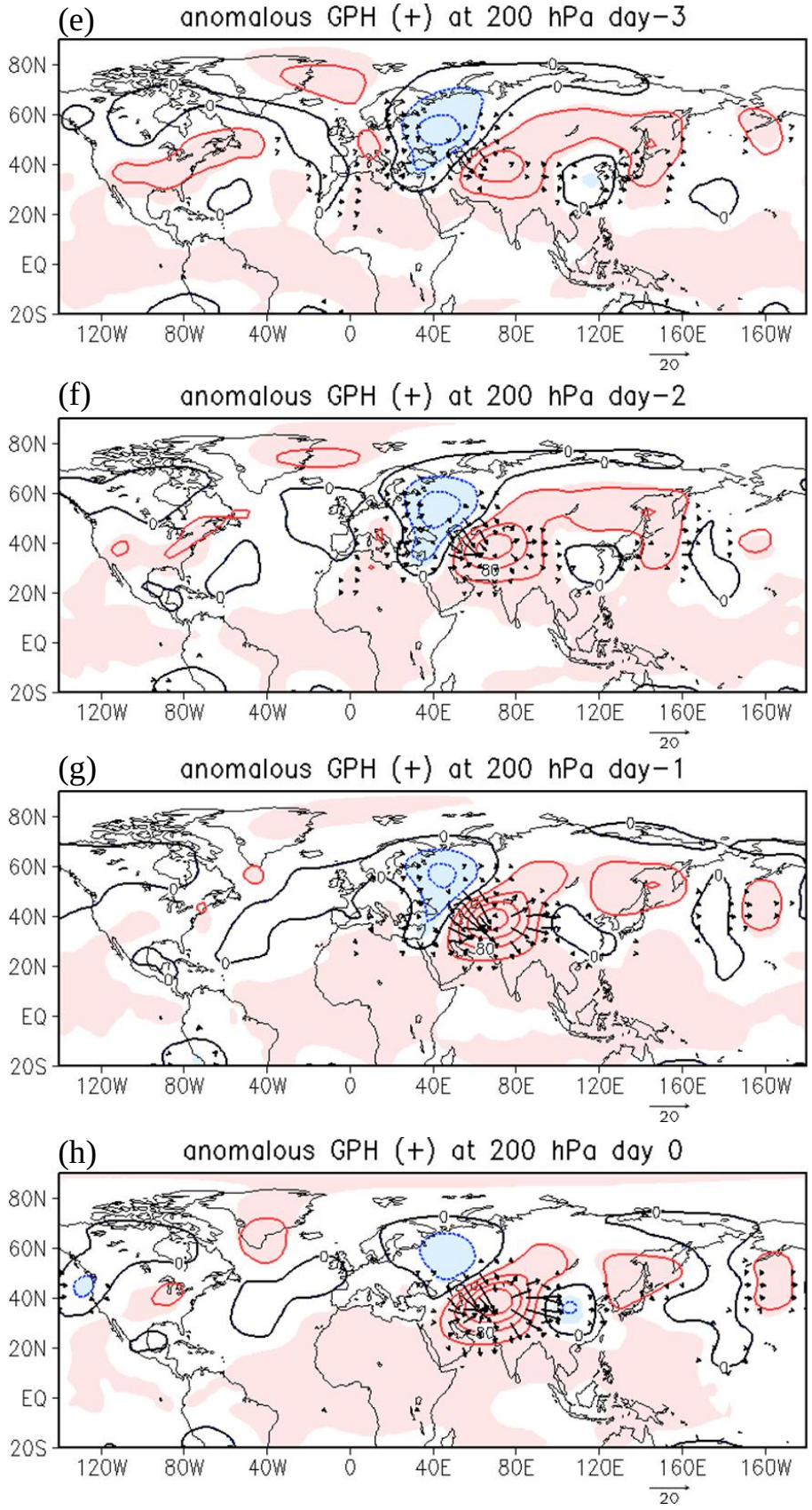

Fig.2.1. Continued.

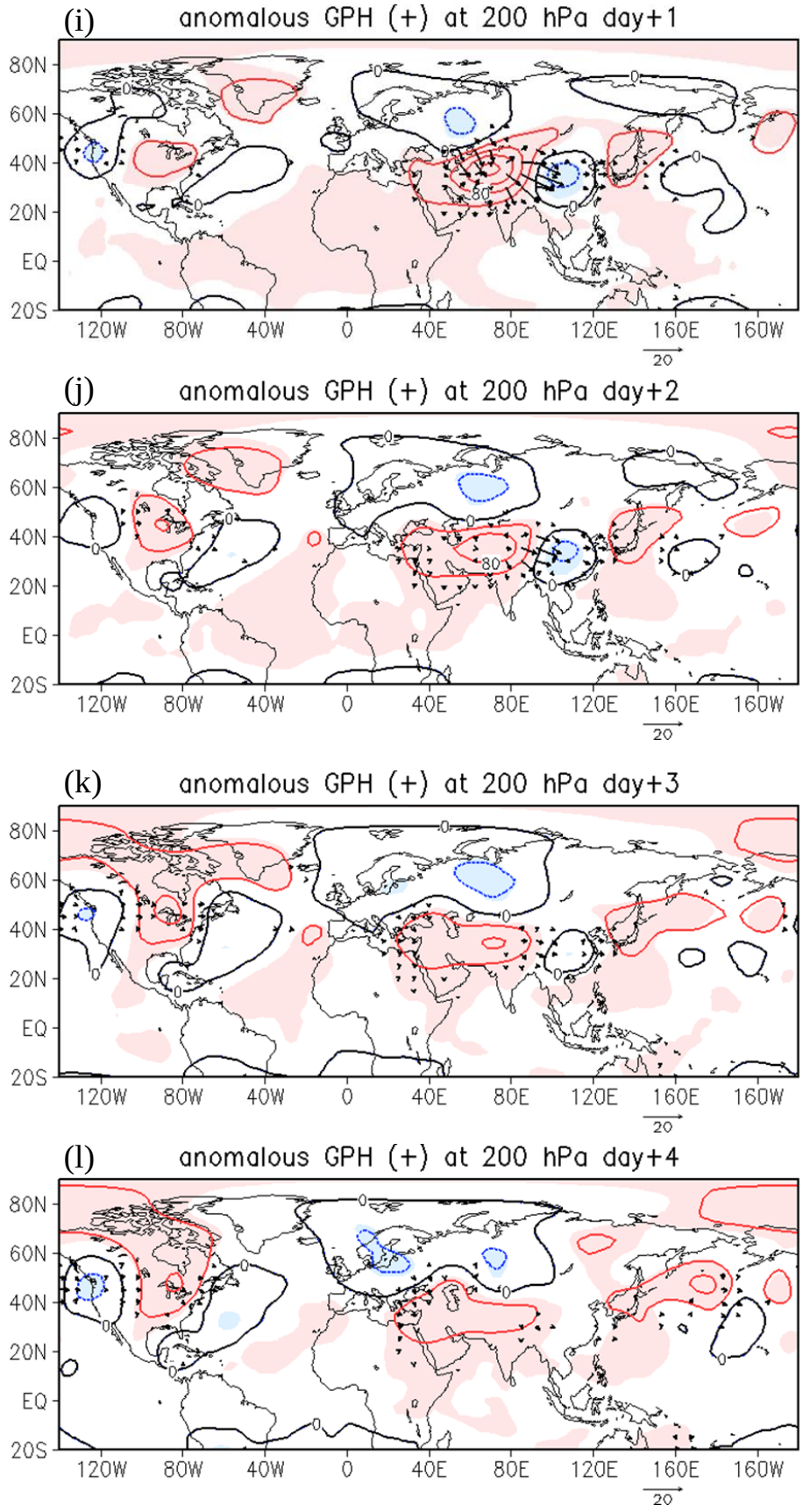

Fig.2.1. Continued.

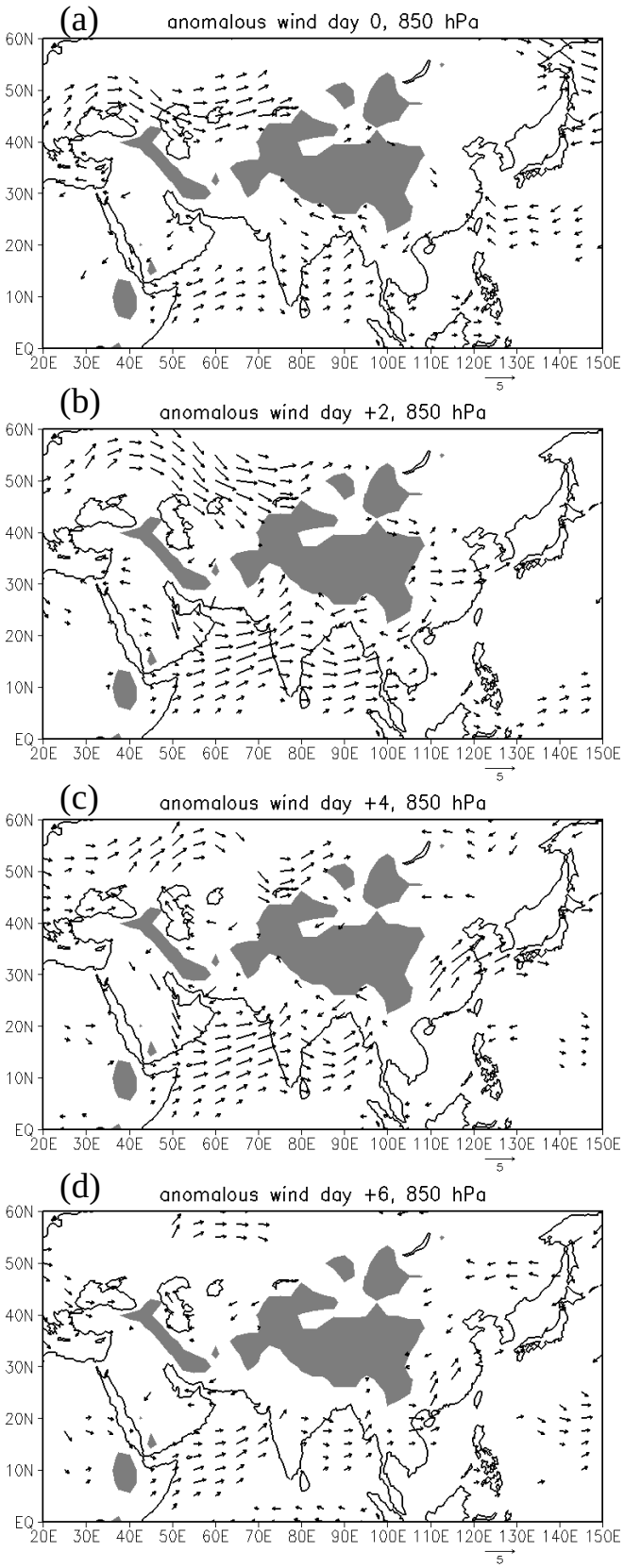

Fig. 2.2. Composite for anomalous horizontal wind at 850 hPa at (a) day 0, (b) day +2, (c) day +4 and (d) day +4. The unit is m s^{-1}. The vector is plotted only at the grid where the value is 95% confidence level.

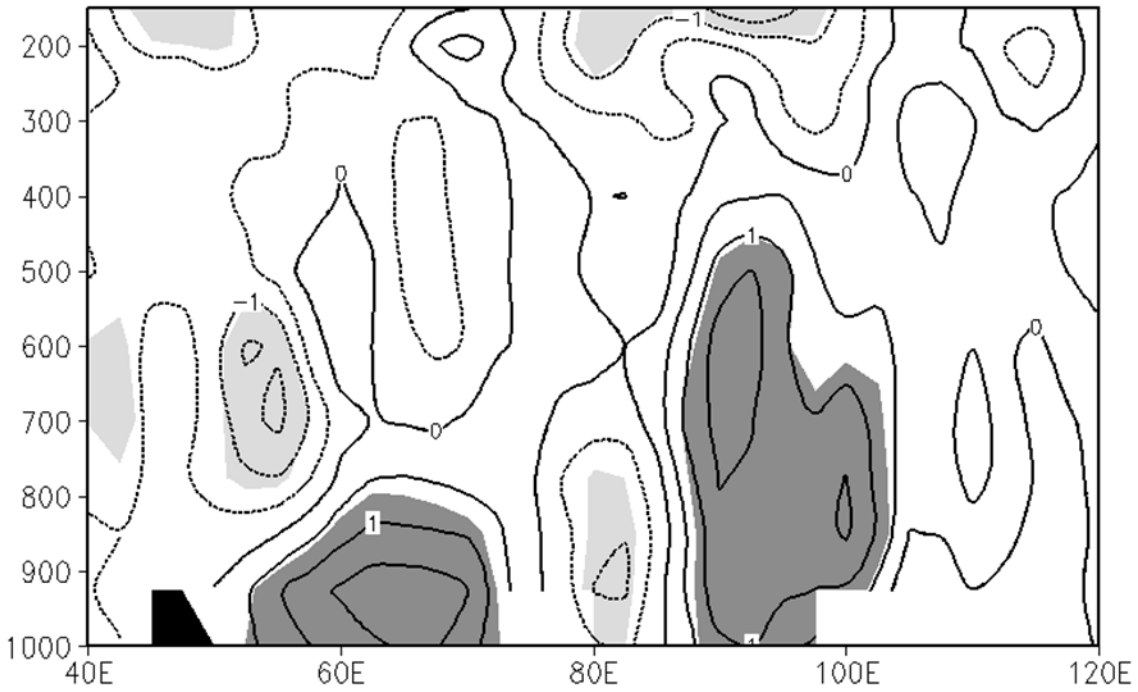

Fig. 2.3. Cross section of composite for anomalous meridional wind speed along 15° N at day +4. Contour interval is 0.5 m s^{-1}

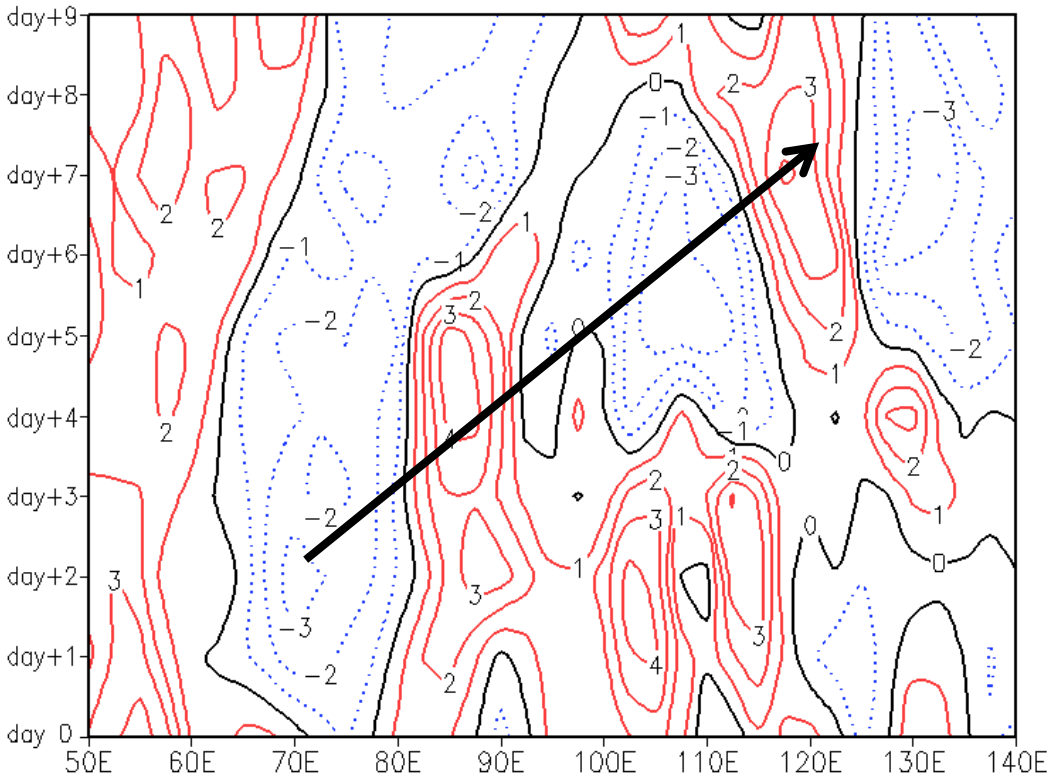

Fig. 2.4. Time-longitude diagram for anomalous vorticity along 15°N at 850 hPa. Contour interval is 1×10^{-5} s^{-1}. The bold line with an arrow head represents the propagation path of low-level wave like disturbance.

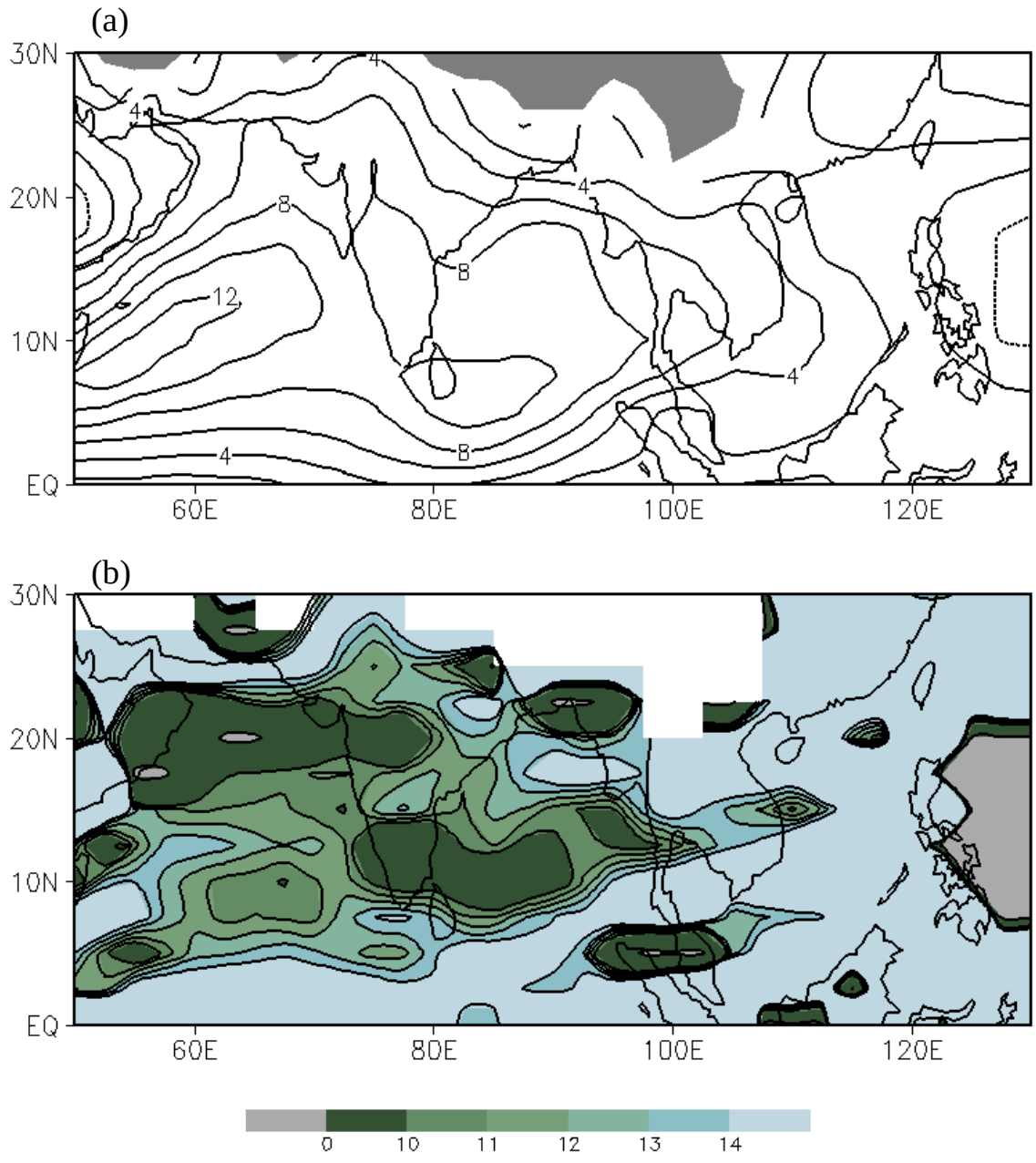

Fig. 2.5. (a) Composite for zonal wind speed at 850 hPa averaged between day +2 and day +7. Contour interval is 2 m s^{-1}. (b) The wave number of the stationary Rossby wave calculated from (a).

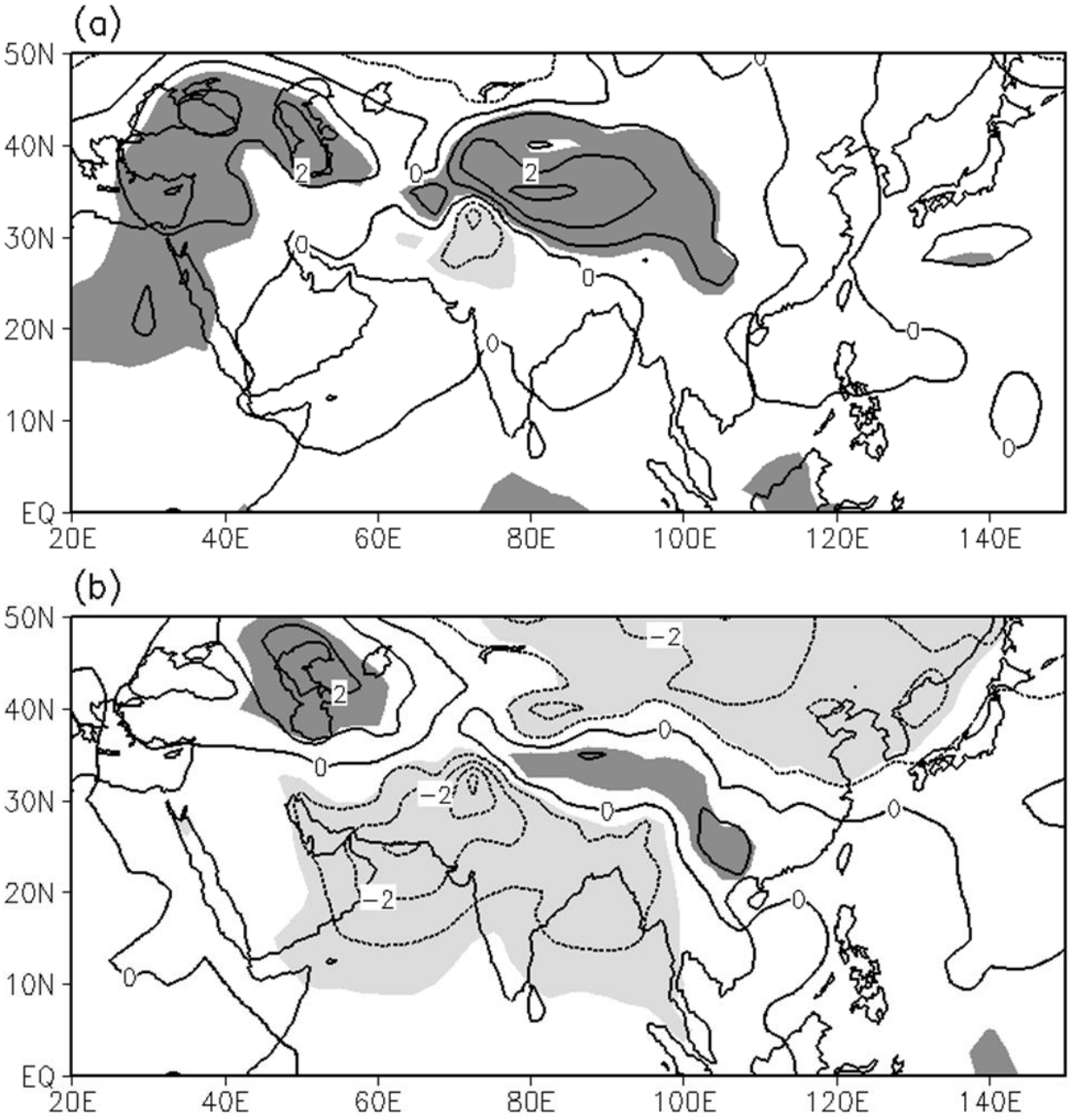

Fig. 2.6. Composite for anomalous surface pressure. Contour interval is 1 hPa.

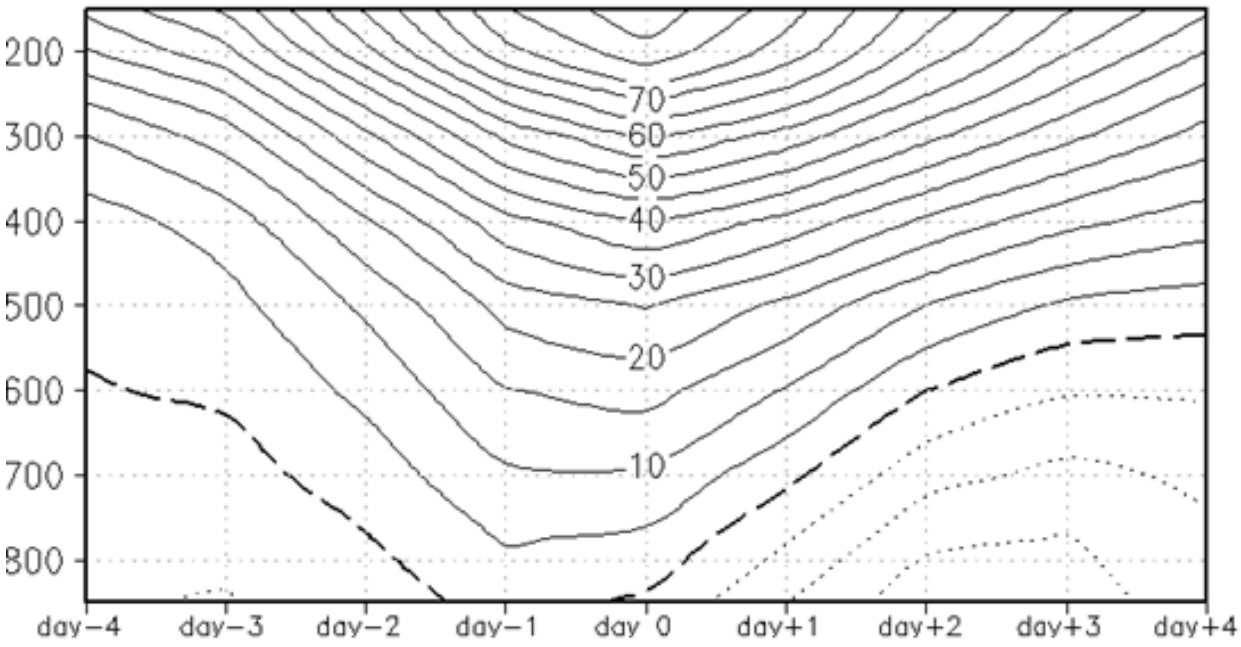

Fig. 2.7. Time–pressure diagram for the composite of anomalous GPH averaged over the low pressure area (62.5°-72.5°E, 25°-30°N). Contour interval is 5 m.

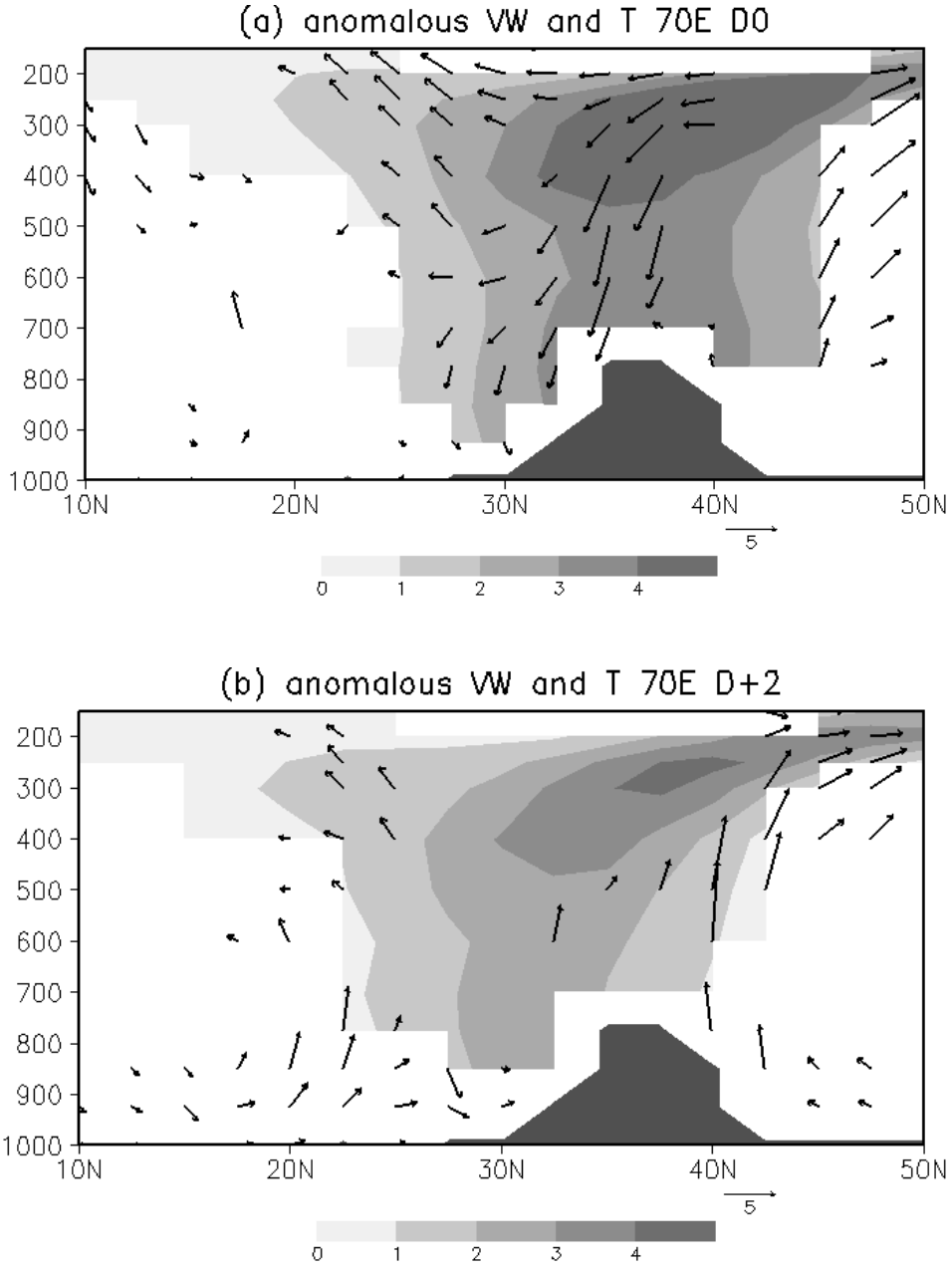

Fig. 2.8. Latitude–pressure cross sections along 70°E for composites of anomalous meridional and vertical wind (vectors), and anomalous temperature (shading) at (a) day 0 and (b) day +2. The vertical wind component is multiplied by -100.

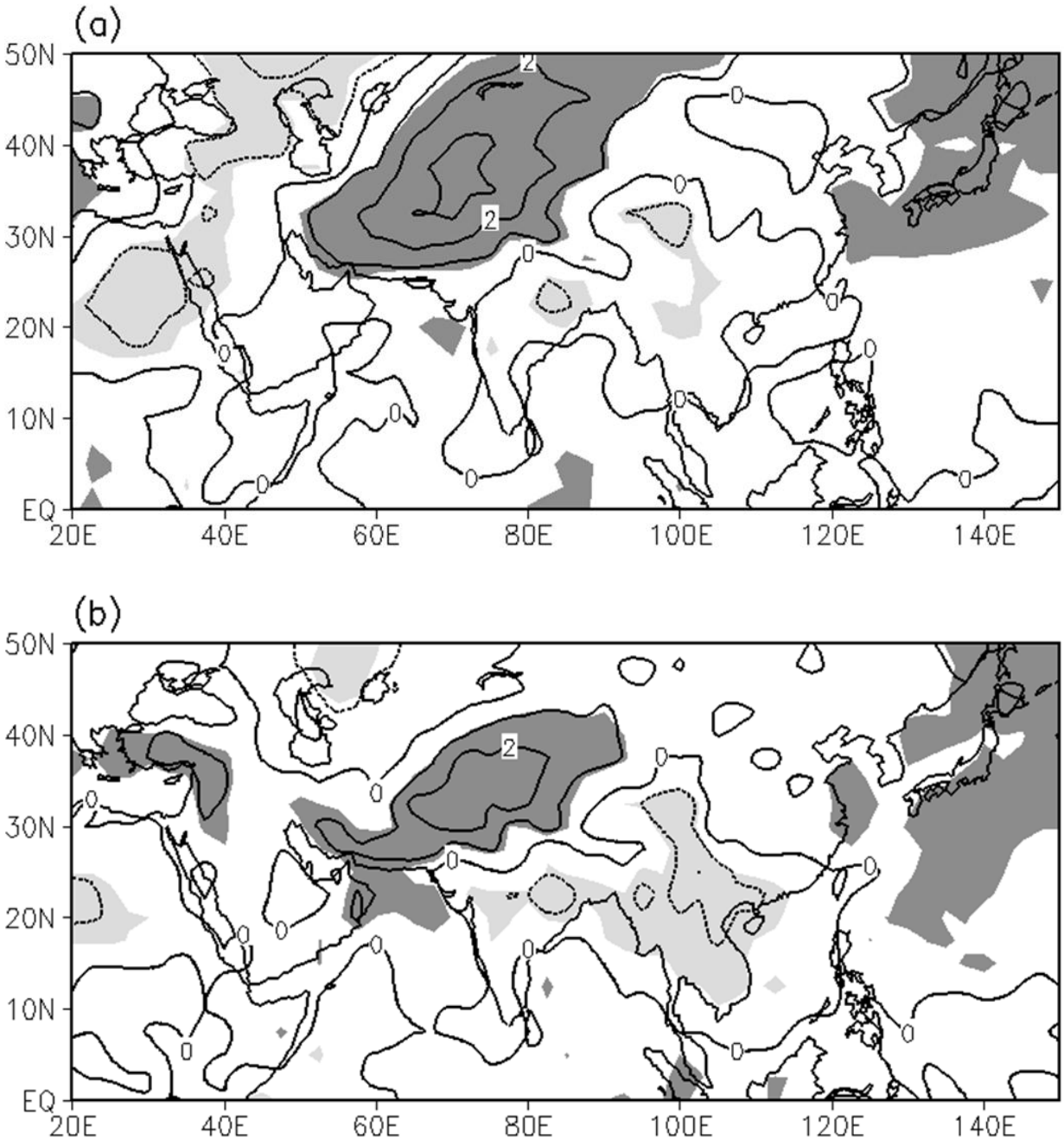

Fig. 2.9. Composite for temperature at a height of 2 m at (a) day 0 and (b) day +2. Contour interval is 1 K.

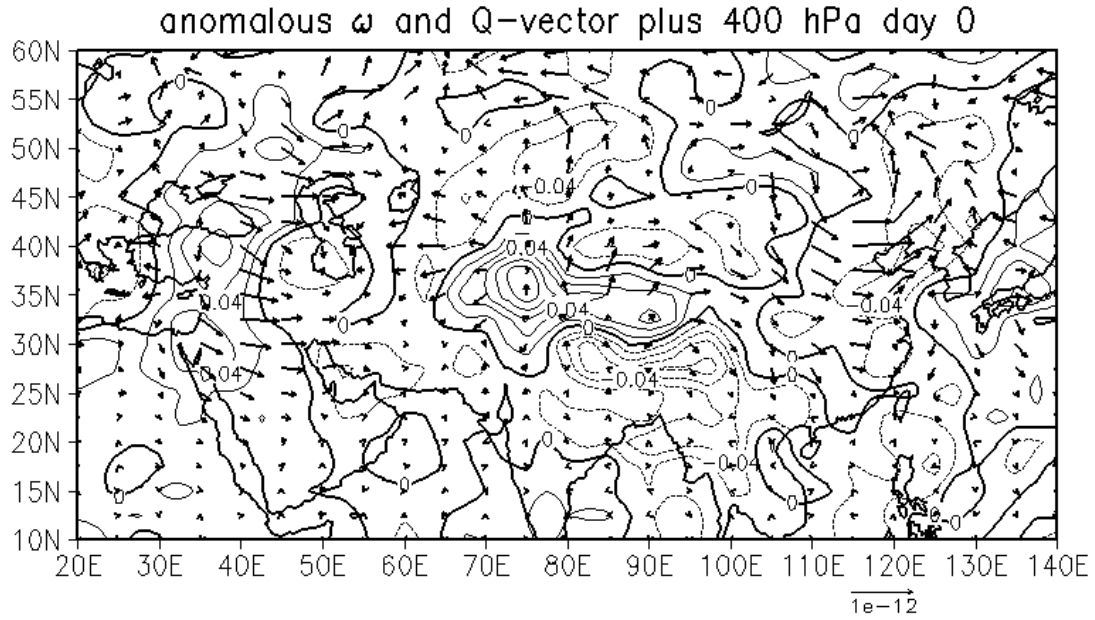

Fig. 2.10. Composites for anomalous vertical p velocity (contours; [Pa s^{-1}]) and the Q vector for the anomalous field (vectors; [kg^{-1} m^2 s^{-1}]) at 400 hPa at day 0.

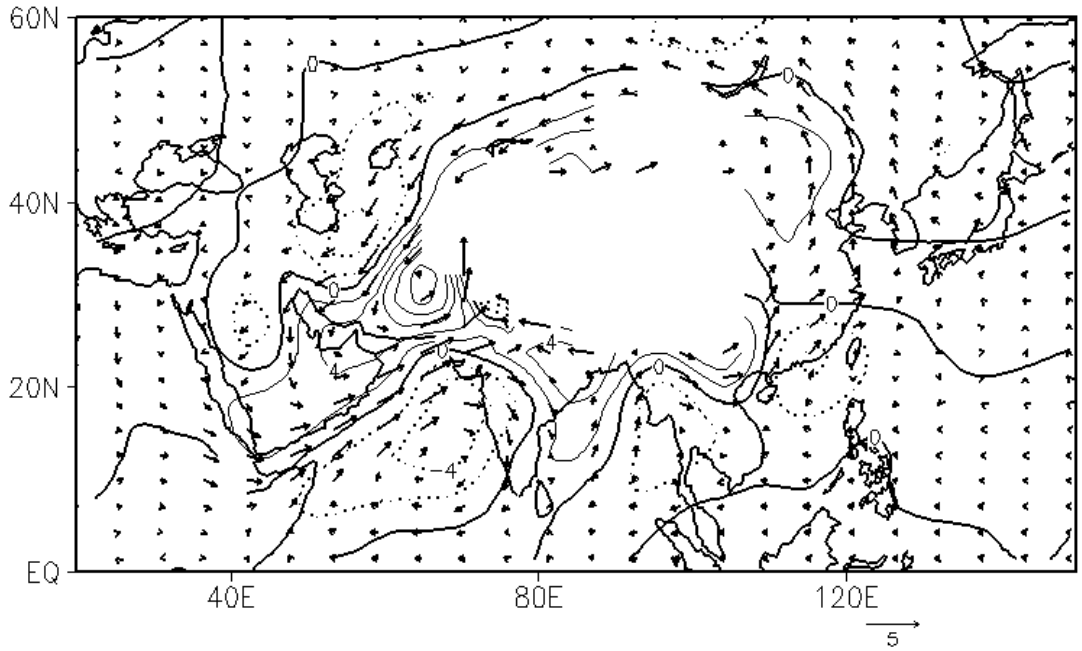

Fig. 2.11. Results from the numerical LBM experiments showing the 30-day average from day 11 to day 40 of the integration. Vector represents the horizontal wind. The unit of vector is m s^{-1}. Contours represent the vorticity. Contour interval is 2×10^{-6} m.

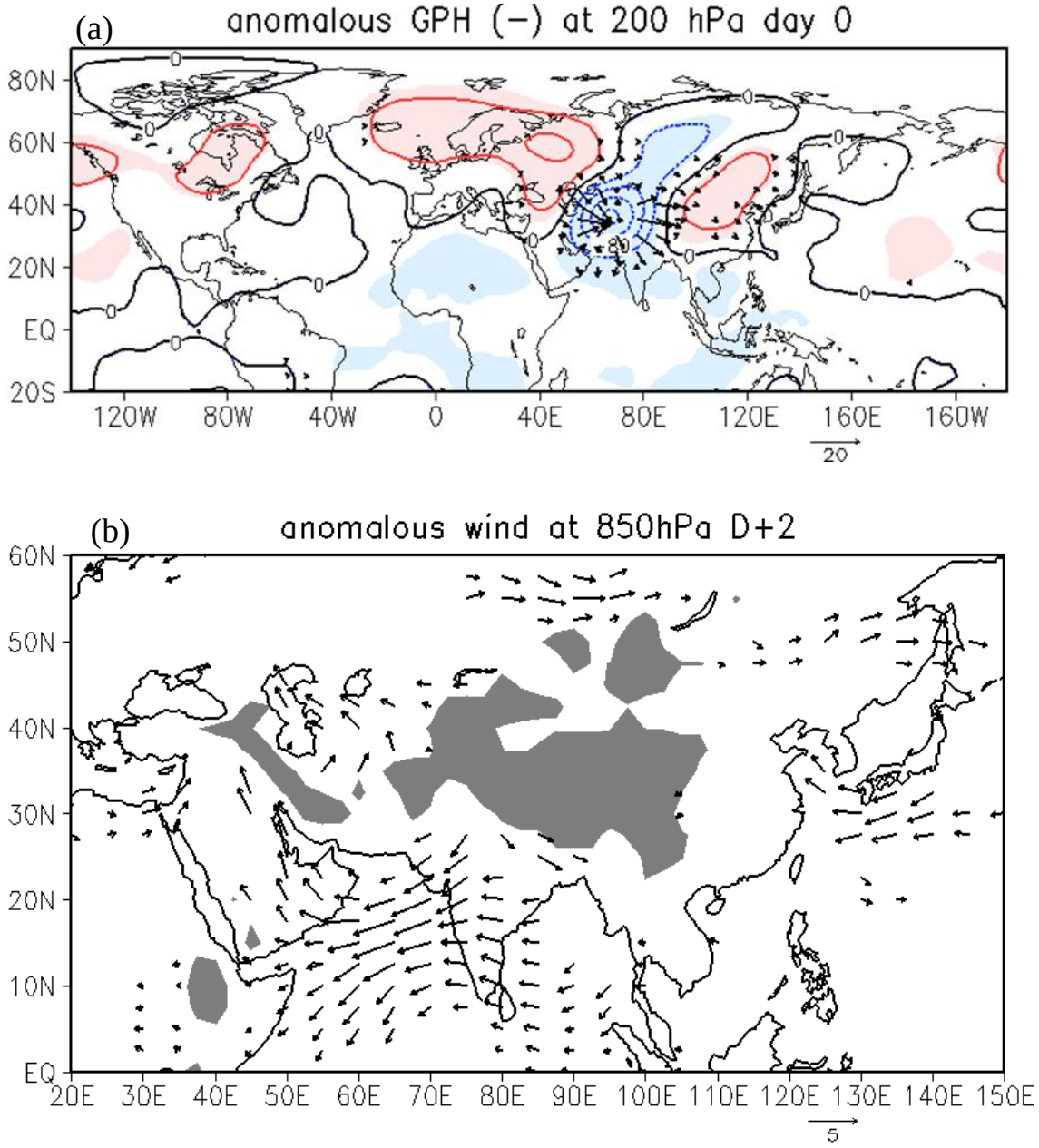

Fig. 2.12. (a) As Fig. 2.1, but for negative composite at day 0. (b) As Fig. 2.2, but for negative composite at day +2.

3. The variation of weather over the Asian monsoon region related to the variation of geopotential height over the western Tibetan plateau

In this chapter the variation of weather over the Asian monsoon region related with the variation of geopotential height over the western Tibetan plateau is investigated. Variations of precipitation and temperature are focused on.

3.1. Method

Composites are computed with the same procedure as chapter 2. To investigate variations related to the variation of geopotential height over the western Tibetan plateau the difference between positive and negative composites is analysed.

The two-sided Wilcoxon–Mann–Whitney rank sum test is used in significance tests for precipitation and OLR data because the distributions of precipitation and OLR are non-Gaussian and resemble the Gamma distribution.

3.2. Results

Figure 3.1 shows difference between positive and negative composites for OLR averaged for 5 days. Between day –9 and day –5, the first pentad centered at day –7, the negative OLR anomalies are seen over the northern Indian Ocean, and South and Southeast Asia (Fig. 3.1a). The positive OLR anomaly is seen over Central America. OLR anomalies are also distributed over North America. OLR anomalies with alternate signs are seen along the wave train propagation route from the northern Atlantic Ocean to the western Tibetan

Plateau in the first and second pentads (Fig. 3.1a and 3.1b). The negative OLR anomalies of more than 20 W m^{-2} over the northern Indian Ocean move northward, and extend across the Arabian Sea, the Indian subcontinent, the Bay of Bengal, Southeast Asia, and south China (Fig. 3.1b). The positive OLR anomaly over the western Tibetan Plateau is intensified simultaneously. Between day +1 and day +5; i.e., in the third pentad, the negative OLR anomaly persists from the northern Arabian Sea to south China (Fig. 3.1c) , and a positive OLR anomaly appears over the central Indian Ocean.

The composite for precipitation is consistent with that for OLR over most of Asia, and shows a more detailed distribution of anomalies than OLR (Fig. 3.2). An increase in precipitation appears along the west coast of the Indian subcontinent, and this enhanced precipitation is retained there for about two weeks. A marked increase in precipitation is seen along the southern foothills of the Tibetan Plateau from day +1 to day +5 (Fig. 3.2c). At the same time, an increase in precipitation is seen along the western coast of Southeast Asia and Myanmar. The negative anomaly around the Yangtze River basin is intensified. Precipitation over South Asia increases about a week before, and after day 0.

Figure 3.3 shows time-series of composite difference for precipitation averaged over South Asia (70°-90°E, 10°-30°N) and Southeast Asia (90°-110°E, 10°-25°N). The positive/negative composite shows the increase/decrease of the average precipitation over both South and Southeast Asia respectively. Precipitation tends to increase over the southern part of South Asia (south to 20°N) before day 0, while precipitation increases over the northern part of South Asia after day 0 (Fig. 3.2). The Average precipitation over Southeast Asia increases sharply after day 0 and reaches about 3mm day^{-1} at day +2 (Fig. 3.3b).

Figure 3.4 shows the composite difference for velocity potential at 200 hPa and 850 hPa. The anomalous divergent wind is consistent with the variations in OLR and precipitation (Fig. 3.1 and 3.2). The disturbance in the tropics, which has the structure of wave number 1, is seen from the first to the last pentad, and migrates eastward. During the first pentad, an area with active convection is centered on the Indian Ocean, and another area with suppressed convection is centered on Central America (Fig. 3.4a). The active convection over the northern Indian Ocean causes convergence over Central Asia and the Tibetan Plateau where the developed

anticyclonic anomaly is located (Fig 3.4a and 3.4b). As shown by Rodwell and Hoskins (1995) and Zhang et al. (2004), the convection over South and Southeast Asia is related to the anomaly over Central Asia and the western Tibetan Plateau. We will confirm this relationship using a numerical LBM experiment in Section 4. Part of the active convection moves to Southeast Asia and converges to the north between day +1 and day +5, which may cause the decrease in precipitation over the Yangtze River basin (Fig. 3.2c and 3.4e). The anomaly in the tropics moves eastward with 35-40 days period (Fig. 3.5).

Figure 3.6 shows the composite difference for temperature at a height of 2 m averaged for 5 days. The positive and negative temperature anomalies are distributed from the northern Atlantic Ocean to the western Tibetan Plateau alternately (Fig. 3.6a and 3.6b). The black body emission can be estimated from the Stefan-Boltzmann law: $Q = \sigma T^4$, where σ is Stefan-Boltzmann's constant and T is the black body's temperature. The estimated black body emission anomaly (Fig. 3.7a and 3.7b) calculated from the composite for temperature at a height of 2 m along the wave propagation route from the North Sea to the western Tibetan Plateau is comparable with the composites for OLR (Fig. 3.1a and 3.1b). The variation in temperature near the surface from the North Sea to the western Tibetan Plateau is due to the weather conditions under the high/low pressure systems. The OLR anomaly along the wave propagation route seems to mainly reflect the surface temperature anomaly. The positive temperature anomaly from the Iranian plateau to the western Tibetan Plateau is seen between day –4 and day +5 (Fig. 3.6b and 3.6c). These regions are arid. The positive temperature anomaly is caused by the upper-level anticyclonic anomaly, and is connected with the intensification of the heat-low at low levels. The negative temperature anomaly from South Asia to Southeast Asia is retained from the second to the third pentads (Fig. 3.5b and 3.5c). At the same time, an increase in precipitation and decrease in OLR are seen (Figs 3.1b–c and 3.2b–c). The estimated black body emission over these regions is not at all consistent with the OLR anomaly (Fig. 3.7b and 3.7c). A large negative OLR anomaly indicates well developed cumulus with a high cloud top, and the decrease in near-surface temperature is due to the associated precipitation and cloud cover.

The results of the composite analysis show that the variation in the geopotential height anomaly over the

western Tibetan Plateau is connected to variation in the Asian summer monsoon, and is influenced by two factors. One is the propagation of the wave train from the northern Atlantic Ocean to the western Tibetan Plateau via western Russia. The other is the convection over the northern Indian Ocean, which is related to disturbance with a wave number of 1 in the tropics. The disturbance in the tropics shows similar characteristics to the MJO. Referring to Wheeler and Hendon (2004) and Pai et al. (2011), the composites between day –9 and day –5, and between day –4 and day 0, seem to correspond to phases 3 and 4 of the MJO index when the active convection is over the Indian Ocean (Wheeler and Hendon 2004). The composite between day +1 and day +5 also resembles phase 5 of the MJO index, except the variation from South Asia to Southeast Asia.

3.3. Summary

The variation of weather over the Asian monsoon region related to the variation of geopotential height over the western Tibetan plateau is investigated in the present chapter. The composite analysis with the same procedure as chapter 2 is made. Major results in the present chapter are summarized as follows:

1) Due to the marked positive/negative geopotential height anomaly over the western Tibetan plateau increasing/decreasing of precipitation over South Asia to Southeast Asia is sustained for about a week after day 0, respectively. The variation of precipitation is related to the quasi-stationary low-level Rossby wave which is caused by the marked geopotential height anomaly as shown in Chapter 2.

2) Before the development of the positive geopotential anomaly over the western Tibetan plateau the negative OLR anomaly over the northern Indian Ocean is seen. The composites of velocity potential show the anomaly with wave number 1 in the tropics. The part with active convection of the disturbance is over the Indian Ocean. The negative OLR anomaly before day 0 is due to the disturbance in the tropics. At the same time the part with suppressed convection is from the eastern Pacific Ocean to the Central America. The anomaly of OLR before day 0 resemble that due to the MJO（Matthew and Hendon 2004; Pai et al. 2011).

3) The active convection over the northern Indian Ocean causes low-level-wind convergence over the Central Asia and the Tibetan plateau. It can be said that variation of the anomaly over the western Tibetan plateau is influenced by two factors; the propagation of wave train from the northern Atlantic Ocean and the convection over the northern Indian Ocean. The concurrent occurrence of two factors causes the significant anomaly of geopotential height over the western Tibetan plateau.

4) The negative near-surface temperature anomaly that develops from South Asia to Southeast Asia, and persists from day –4 to day +5, is caused by the cloud cover and precipitation. The variation in temperature near the surface from the North Sea to the western Tibetan Plateau is due to the weather conditions under the high/low pressure systems.

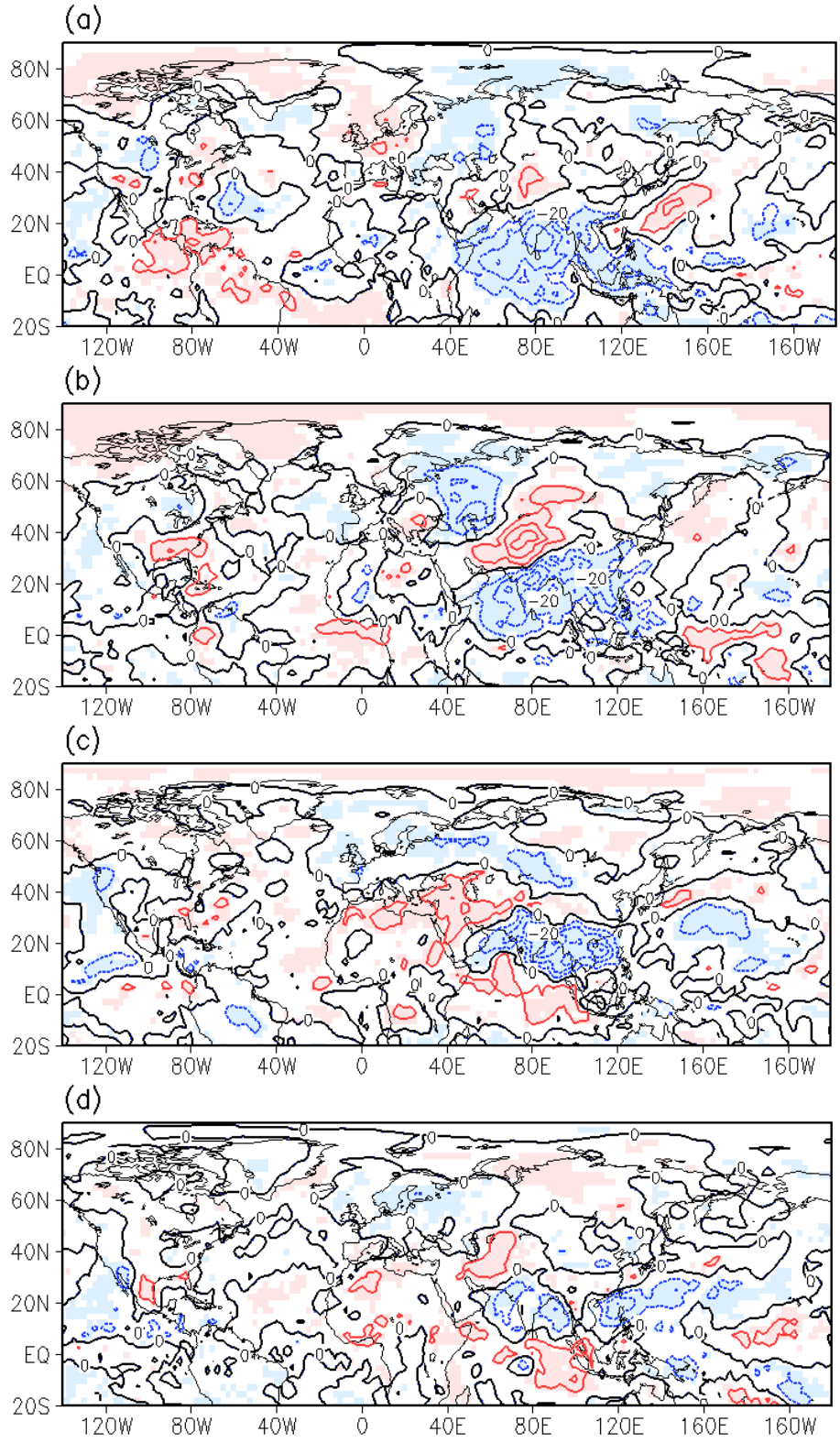

Fig. 3.1. Composite difference for OLR averaged between (a) day -9 and day -5, (b)day -4 and day 0, (c) day +1 and day+5 and (d) day +6 and day+10. Contours represent OLR. Contour interval is 10 W m^{-2}. Shading represents the 95% confidence level.

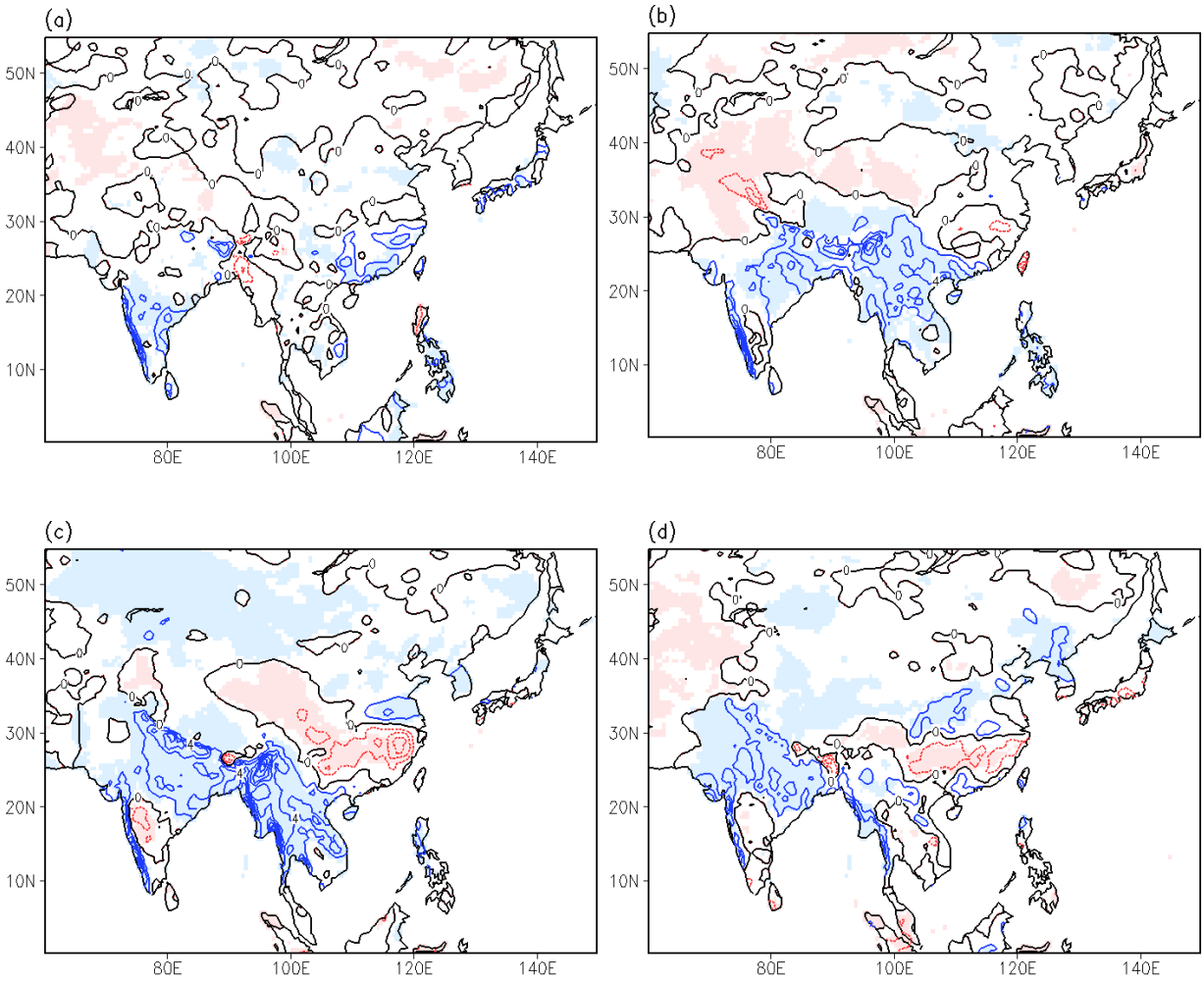

Fig. 3.2. As for Fig. 3.1, but for precipitation. Contour interval is 2 mm day^{-1}.

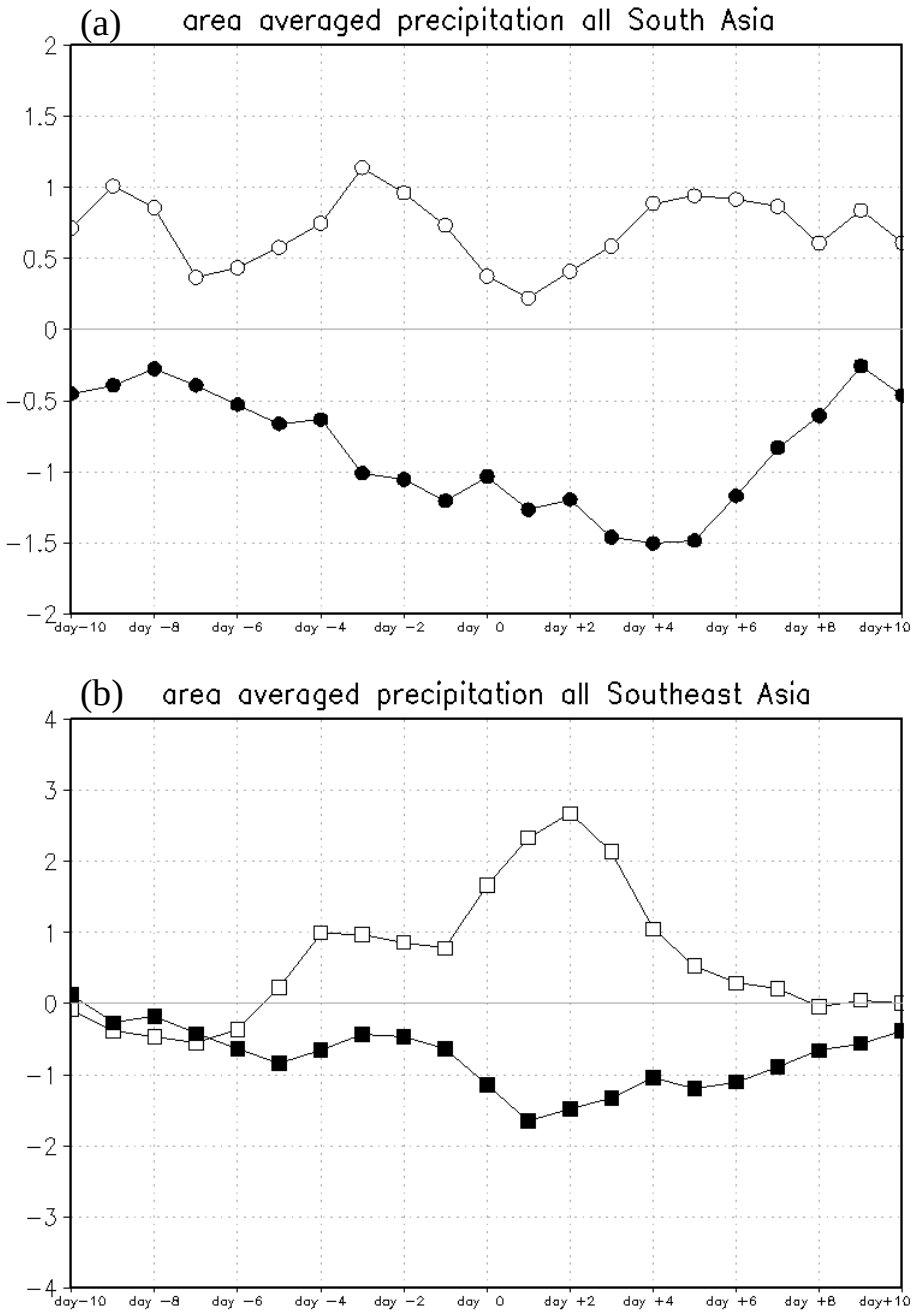

Fig. 3.3. Time series of regionally-averaged composites for precipitation over land (a) over South Asia (70°-90°E, 10°-30°N) and (b) Southeast Asia (90°-110°E, 10°-25°N). Open circle and square is for the positive composite. Closed circle and square is for negative composites.

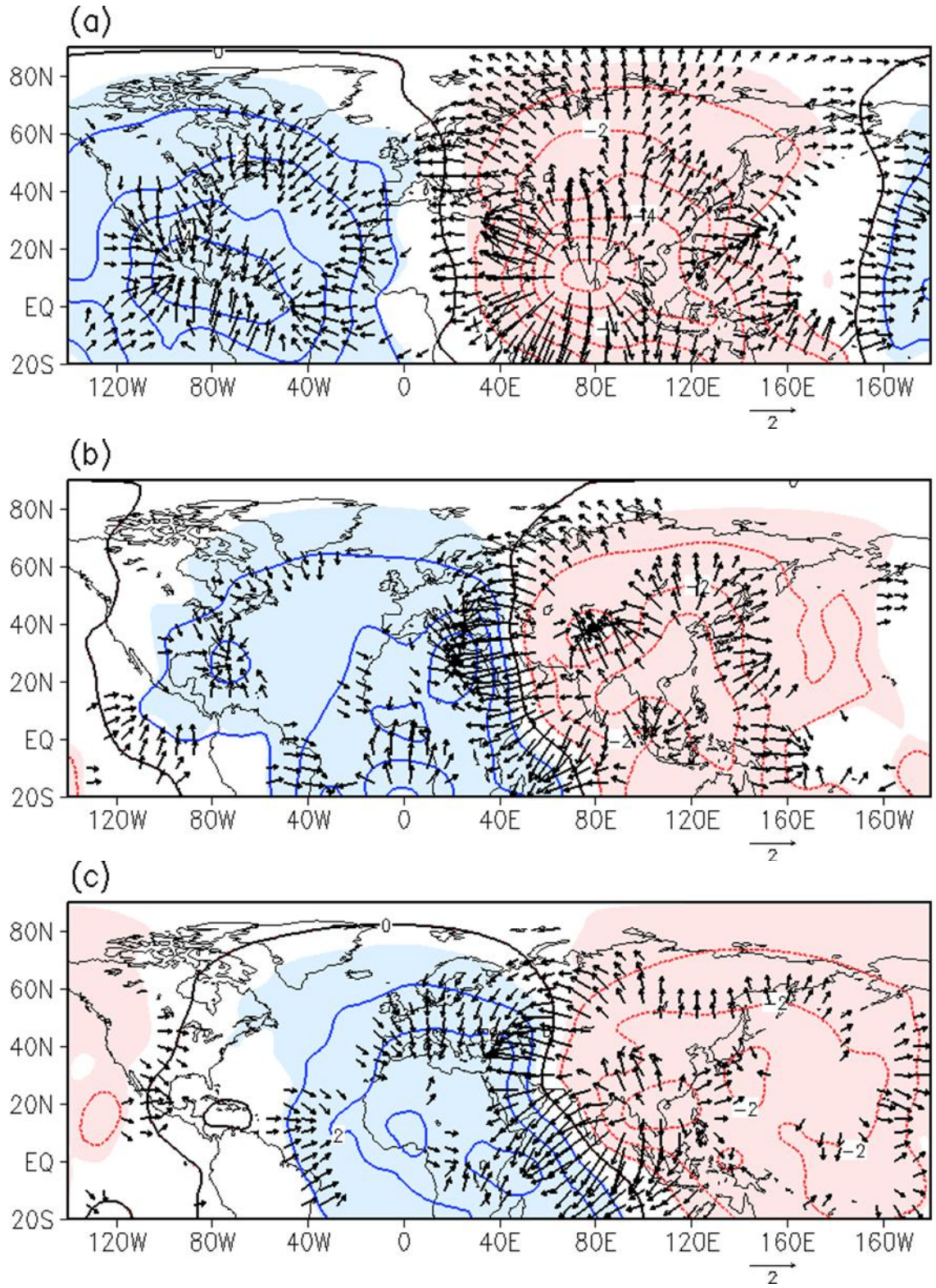

Fig. 3.4. As for Fig. 3.1, but for velocity potential at (a)-(c) 200 hPa and (d)-(f) 850 hPa averaged between (a),(d) day -9~day -5, (b),(e) day -4~day 0 and (c),(f) day +1~day +5. Contour represents velocity potential. Contour interval is 1×10^{6} m^{2} s^{-1}. Arrow represents the divergence wind, and is plotted at grid points where the magnitude of the divergence wind is greater than 0.5 m s^{-1}.

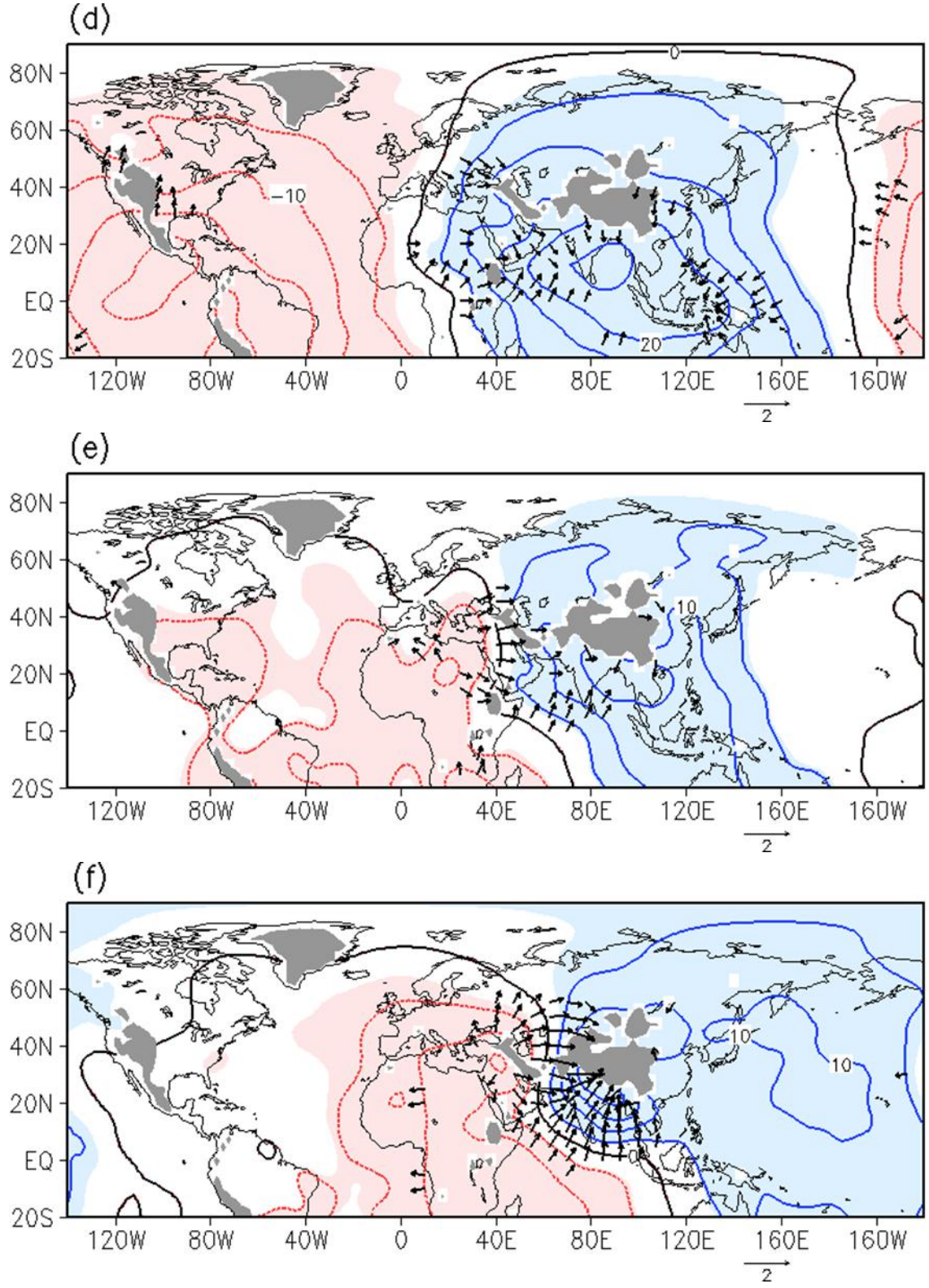

Fig. 3.4. Continued.

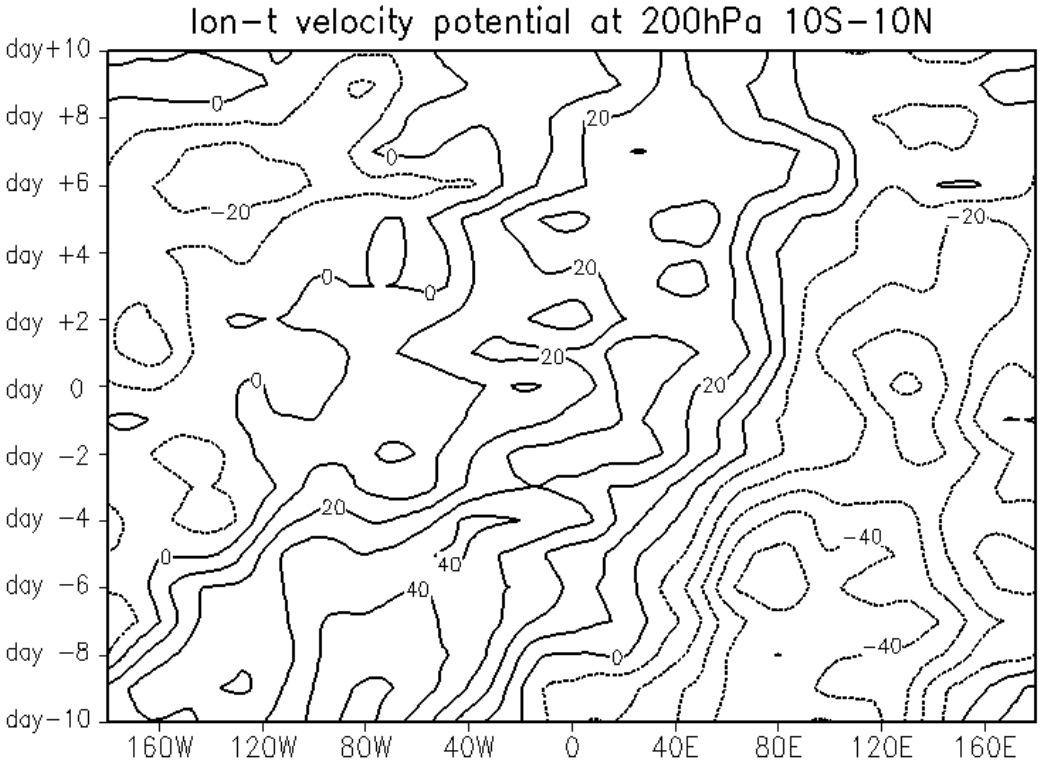

Fig. 3.5. Longitude-time diagram of difference of composite difference for velocity potential at 200 hPa averaged between 10° S and 10° N. Contour interval is 1×10^6 m^2 s^{-1}

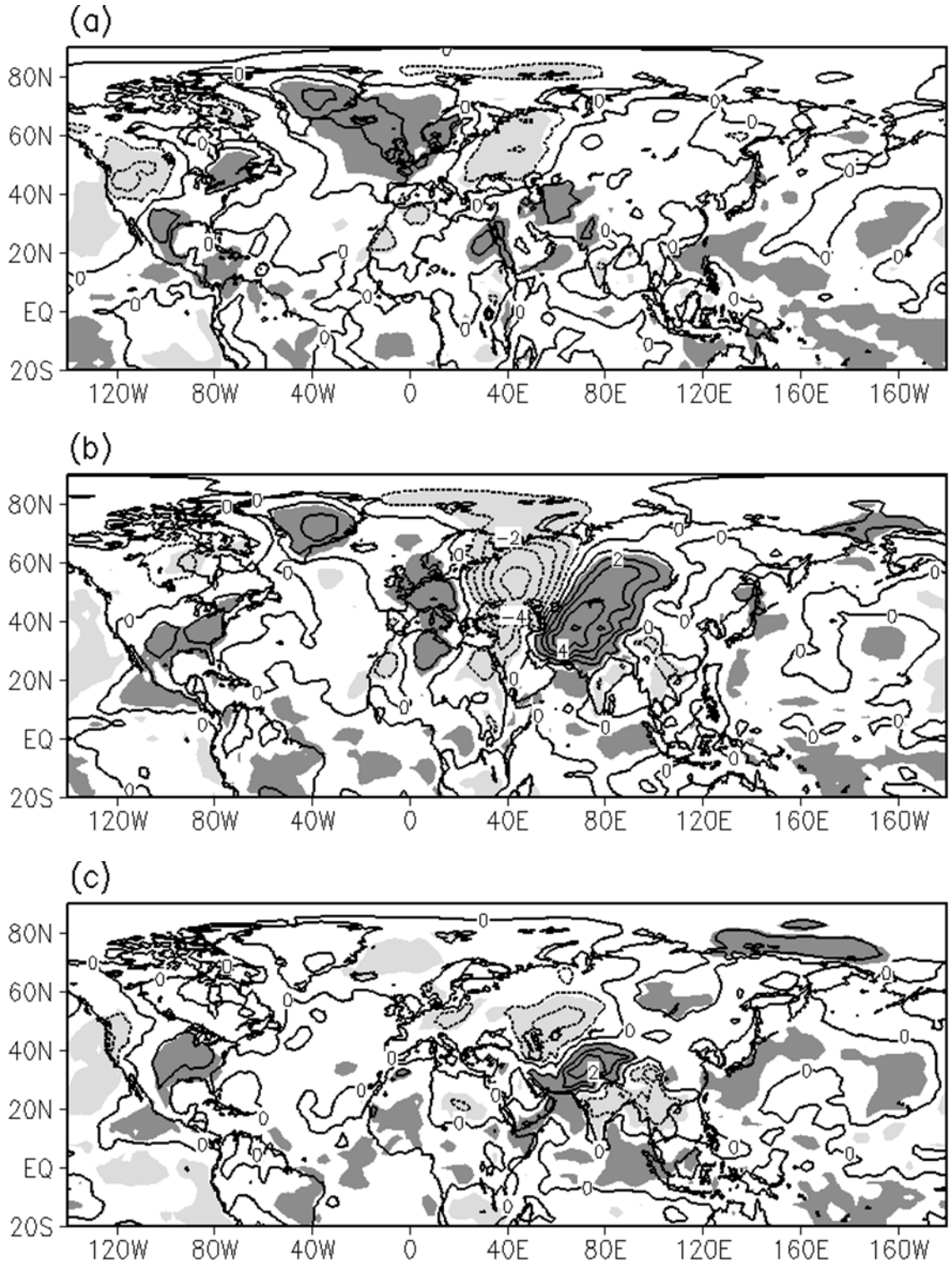

Fig.3.6. As for Fig. 4, but for temperature at a height of 2 m averaged between (a) day -9 and day -5, (b)day -4 and day 0, (c) day +1 and day+5. Contour interval is 1 K.

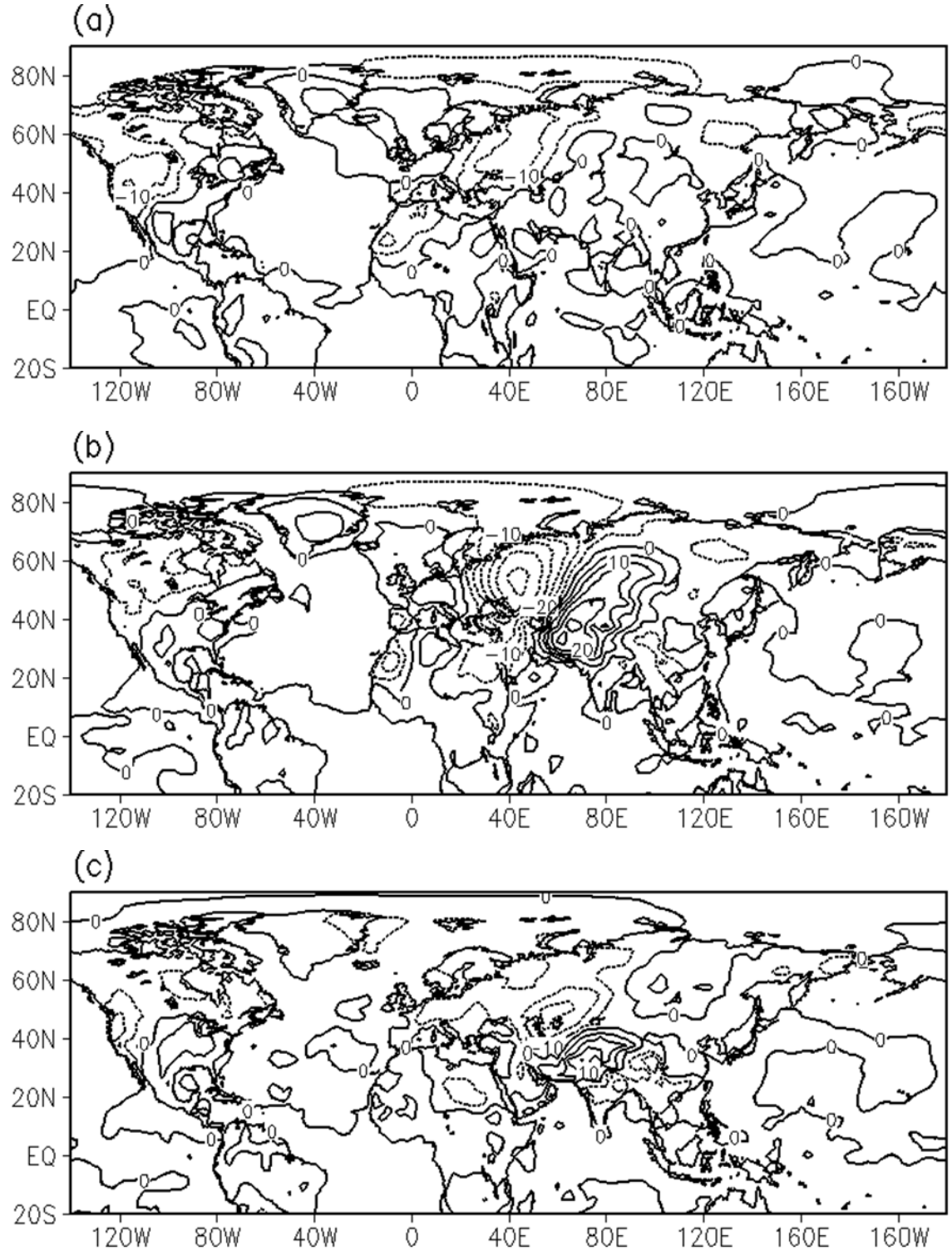

Fig.3.7. As for Fig. 4, but for the black body emission calculated from temperature at a height of 2 m averaged between (a) day -9 and day -5, (b)day -4 and day 0, (c) day +1 and day+5. Contour interval is 5 W m^{-2}.

4. Causes of the marked variation of geopotential height over the western Tibetan plateau

The GPH anomaly over the western Tibetan Plateau is related with two factors; one is the wave train from the middle latitude. The other is the active convection over the Bay of Bengal. In this chapter causes of variation of geopotential height over the western Tibetan plateau are investigated.

4.1. Definition of the ART index

The wave train from the northern Atlantic Ocean passes through the Caspian Sea and arrives at the western Tibetan Plateau (Fig. 2.1). The distribution of the stationary Rossby wave number shows that the Rossby wave propagating in the northern Atlantic-northern Europe wave guide tends to be reflected over the Caspian Sea (Fig.4.1). However there are some openings of wave-guide. The wave-guide is weak over the Caspian Sea, so that the wave activity leaks from the western Russia into the western Tibetan Plateau.

In this section, we consider the propagation of the wave train from the northern Atlantic Ocean to the western Tibetan Plateau. Firstly, we define an index that represents the propagation of the wave train. We selected three areas where the centers of variation of geopotential height along the propagation route are seen: the northern Atlantic Ocean (10°W–10°E, 60°–70°N), western Russia (20°–50°E, 50°–60°N), and the western Tibetan Plateau where the GPH index is defined. The average geopotential height anomaly from daily climatology in each area was calculated and the interannual variation is removed. Finally, the ART (Atlantic, Russia, Tibet) index was defined as a combination of the three standardized area-averaged geopotential height anomalies:

$$\text{ART index}(t) = GPH_A(t-6) - GPH_R(t-2) + GPH_T(t),$$

where GPH_A, GPH_R and GPH_T are the regionally-averaged geopotential height anomaly over the northern

Atlantic Ocean, western Russia and the western Tibetan Plateau, and the number in parentheses denotes the time lag, in days, to the western Tibetan Plateau. This lag is determined by the propagating speed (Fig. 2.1). The term for western Russia is multiplied by –1 because it is out-of-phase to the others. The ART index excludes interannual variations by removing the seasonal average; consequently, it represents the intraseasonal wave propagation. It is also standardized. The positive (negative) ART index represents the propagation from the northern Atlantic Ocean to the western Tibetan Plateau via western Russia with a phase distribution of high–low–high (low–high–low). The absolute value of the ART index reflects the amplitude of the wave train, and its sign shows the phase.

The correlation coefficient between the ART index and the time series of the principal component of the first eigenvector of the variance of geopotential height at 200 hPa over the Tibetan Plateau and surrounding regions (Fig. 1.4) is about 0.6. Although the definition of the ART index is somewhat subjective, the propagation of the wave train from the northern Atlantic Ocean to the Tibetan Plateau is connected to the dominant variation of geopotential height over the Tibetan Plateau and surrounding regions. Composites for more/less than +/–1.5 ART index were calculated using the same procedure as for the GPH index.

4.2. Results of composite analysis concerning the ART index

Figure 4.2 shows the difference between the positive and negative composites associated with the ART index for geopotential height at 200 hPa, and the wave activity flux based on the composite difference for the stream function. The composite of the ART index shows the propagation from the northern Atlantic Ocean to the western Tibetan Plateau via western Russia well. At day –6, the high and low anomalies are seen over northeast North America and to its east (Fig. 4.2a). The composite of the ART index is used to trace the propagation of the wave train back, and to seek the source of the wave train.

The composite difference for geopotential height averaged between day –12 and day –8 shows a positive anomaly over the northeast of North America (Fig. 4.3a). The wave activity flux shows the propagation of the

wave train from northeast North America to the western Tibetan Plateau. After arriving on the western Tibetan Plateau, the wave train propagates eastward along the Asian subtropical jet (Fig. 4.3b).

Figure 4.4 shows the composite difference for the velocity potential averaged between day –12 and day –8, and Figure 4.5 shows the same composite for OLR. Disturbance with a wave number of 1 is seen in the tropics. The center of active convection is over the Indian Ocean, and the center of suppressed convection is over the central Pacific Ocean, Central America, and the Caribbean Sea. (Fig. 3.4). It is suggested that the marked wave train from northeast North America to the western Tibetan Plateau is related to the MJO-like disturbance.

Barlow and Salstein (2006) and Lorenz and Hartmann (2006) showed that precipitation over Central America is strongly influenced by the MJO. It is most likely that OLR anomalies from the eastern equatorial Pacific Ocean to Central America are related to the MJO-like disturbance. The tropical convection may act as a Rossby-wave source (Sardeshmukh and Hoskins 1988). We suggest that the anomalous divergence/convergence caused by the variation in convection over the Eastern Pacific Ocean and Central America is the source of the wave train from northeast North America to the western Tibetan Plateau.

4.3. Numerical experiments using the LBM

To investigate whether the variation in convection over Central America and the northern Indian Ocean, expected from the OLR composites (Figs. 3.1 and 4.5), caused the variation in geopotential height over the western Tibetan Plateau, two numerical experiments based on the LBM were carried out as follows.

In the first experiment, an elliptic heat source, with a horizontal 10° radius of –8 K/day was placed over Central America (centered at 90°W, 20°N), with its maximum at around 500 hPa, and was sustained for the integration period. This thermal forcing mimics the suppressed convection over Central America (Fig. 4.5). Atmospheric states were relaxed to the climatology in May and June. The results show the propagation of a wave train from Central America to the western Tibetan Plateau (Fig. 4.6a). The location of each high and low is consistent with composites for the GPH and ART indexes, and show that variations caused by the tropical

disturbance over Central America can contribute to the generation of an ART wave train with the correct phase. However, anomalies over the northern Atlantic Ocean, western Russia, and the western Tibetan Plateau are not large enough to explain the observed values. It is likely that other dynamical processes, such as transient wave forcing and/or a wave train from another source, reinforces the anomaly over the north Atlantic.

The second numerical experiment followed the same procedure as the first, except that the thermal forcing was now located over the Indian Ocean (90°E, 5°N) to establish the relationship between the geopotential height anomaly over the western Tibetan Plateau and the variation in convection over the Indian Ocean in early summer. The results showed an anomalous high over the western Tibetan Plateau, and eastward propagation of the wave train (Fig. 4.6b).

Consequently, the effect of disturbances in the tropics and middle latitudes tends to be concentrated on the western Tibetan Plateau. When a large-scale disturbance develops in the tropics, such as the MJO, and the associated active/suppressed convection is located over the Indian Ocean/Central America, a large positive geopotential height anomaly is likely to develop over the western Tibetan Plateau.

4.4. Summary

Causes of the marked variation of geopotential height over the western Tibetan plateau are investigated in this chapter. The ART index is defined as the combination of area-averaged geopotential height anomalies over the northern Atlantic Ocean, the western Russia and the western Tibetan plateau. The ART index represents the propagation of wave train from the northern Atlantic Ocean to the western Tibetan plateau via the western Russia. The major results in this chapter are summarized as follows:

1) The wave train that arrives on the western Tibetan Plateau can be traced back to northeastern North America at day –10. A disturbance with a wave number of 1 in the tropics is seen, and is accompanied by positive and

negative OLR anomalies over Central America and the Indian Ocean, respectively. The OLR anomaly over Central America is thought to be the source of the wave train from northeastern North America.

2) Two numerical experiments based on the LBM were completed to assess the role of tropical heat sources in the variation of geopotential height over the western Tibetan Plateau. In the first experiment, the thermal forcing was located over Central America to generate similar wave-train propagation to the composites of the GPH and ART indexes, although the geopotential height anomaly over the western Tibetan Plateau was weak. In the second experiment, the thermal forcing was located over the Indian Ocean, and this also produced a positive geopotential height anomaly over the western Tibetan Plateau. Consequently, tropical heat sources associated with MJO-like wavenumber 1 disturbances constructively generate the height anomaly over the western Tibetan Plateau. The positive (negative) geopotential height anomaly over the western Tibetan Plateau develops when convection is active (suppressed) over the Indian Ocean, and suppressed (active) over the eastern Pacific Ocean and Central America.

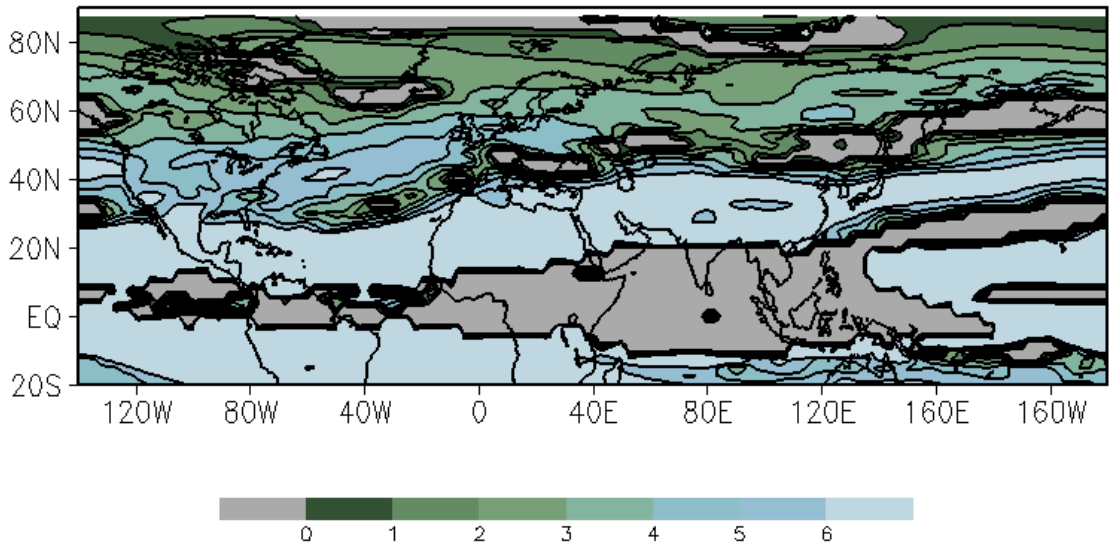

Fig. 4.1. As for Fig. 2.5, but for the stationary Rossby wave number at 200 hPa. The wave number is calculated from the zonal wind speed averaged from day -10 to day 0 of composite for the GPH index.

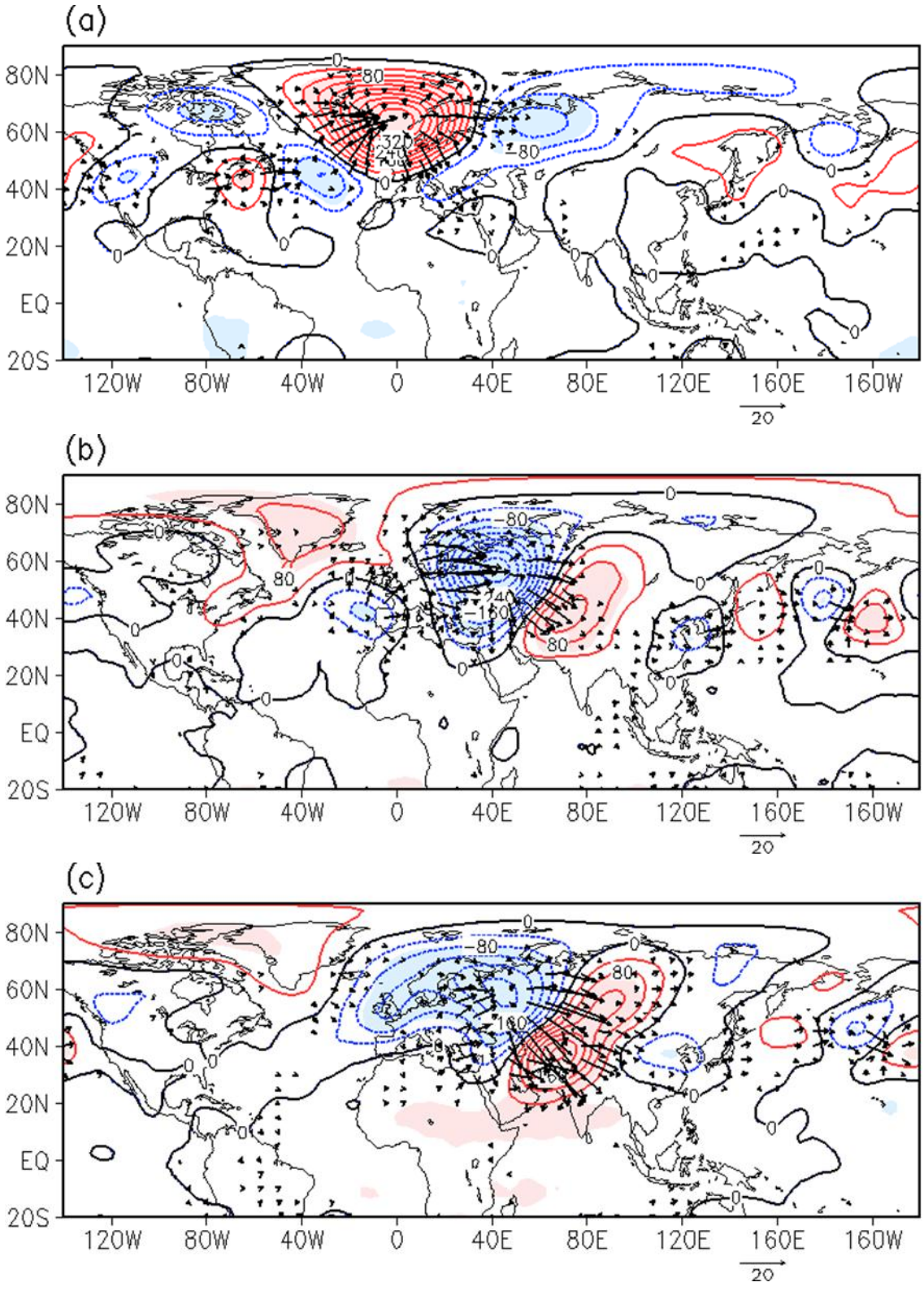

Fig. 4.2. Difference of positive and negative composites for geopotential height at 200 hPa. Contour interval is 40 m. Shade represents statistically 95% confidence level. Arrows represent the wave activity flux, and are plotted at grid points where the magnitude of wave activity flux is greater than 1 $m^2 s^{-2}$.

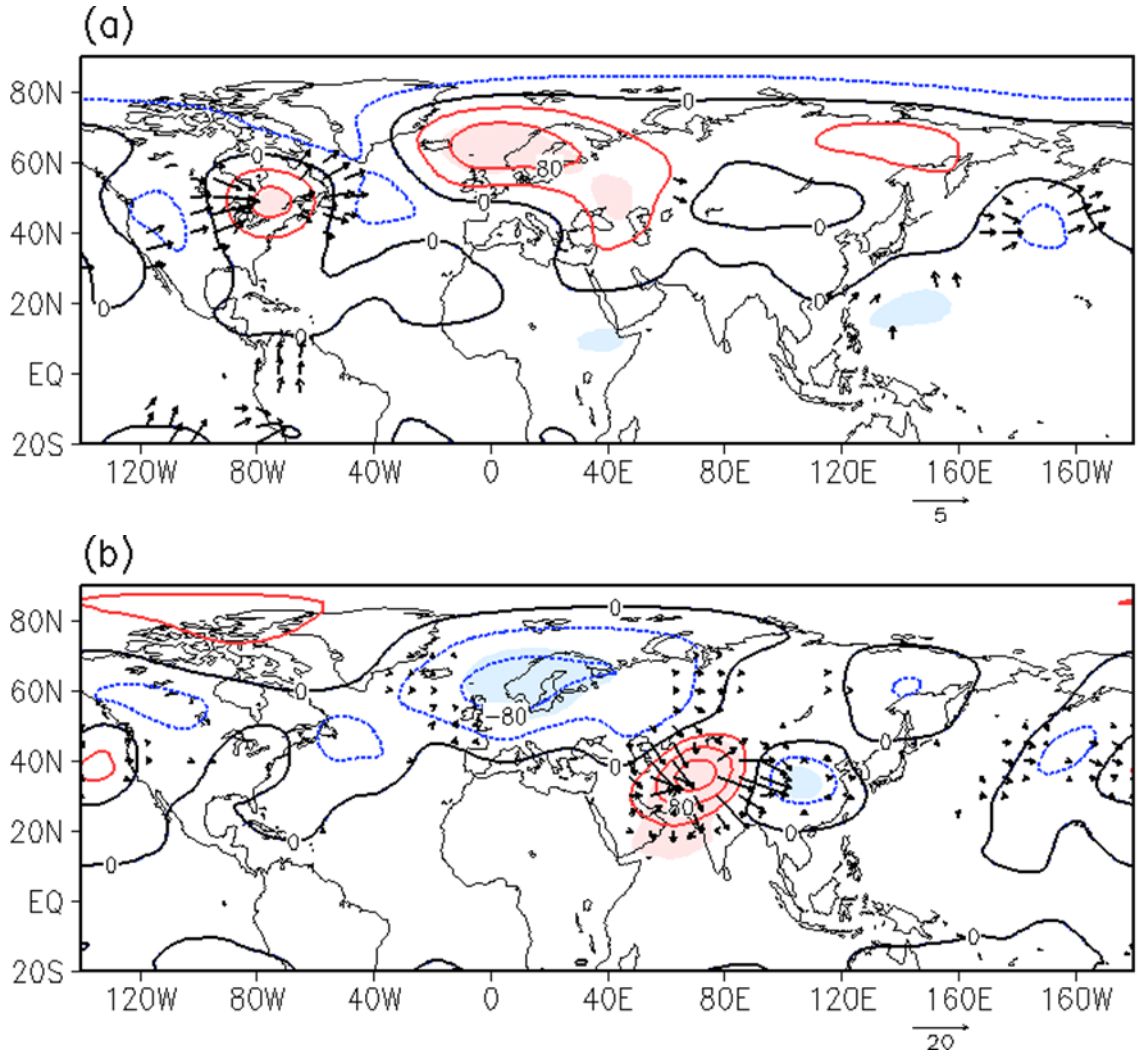

Fig. 4.3. Composite difference for geopotential height at 200 hPa averaged (a) between day -12 and day -8, and (b) between day +1 and day +5. Contour interval is 40 m. Shade represents statistically 95% confidence level. Arrows represent the wave activity flux, and are plotted at grid points where the magnitude of wave activity flux is greater than 1 $m^2 s^{-2}$.

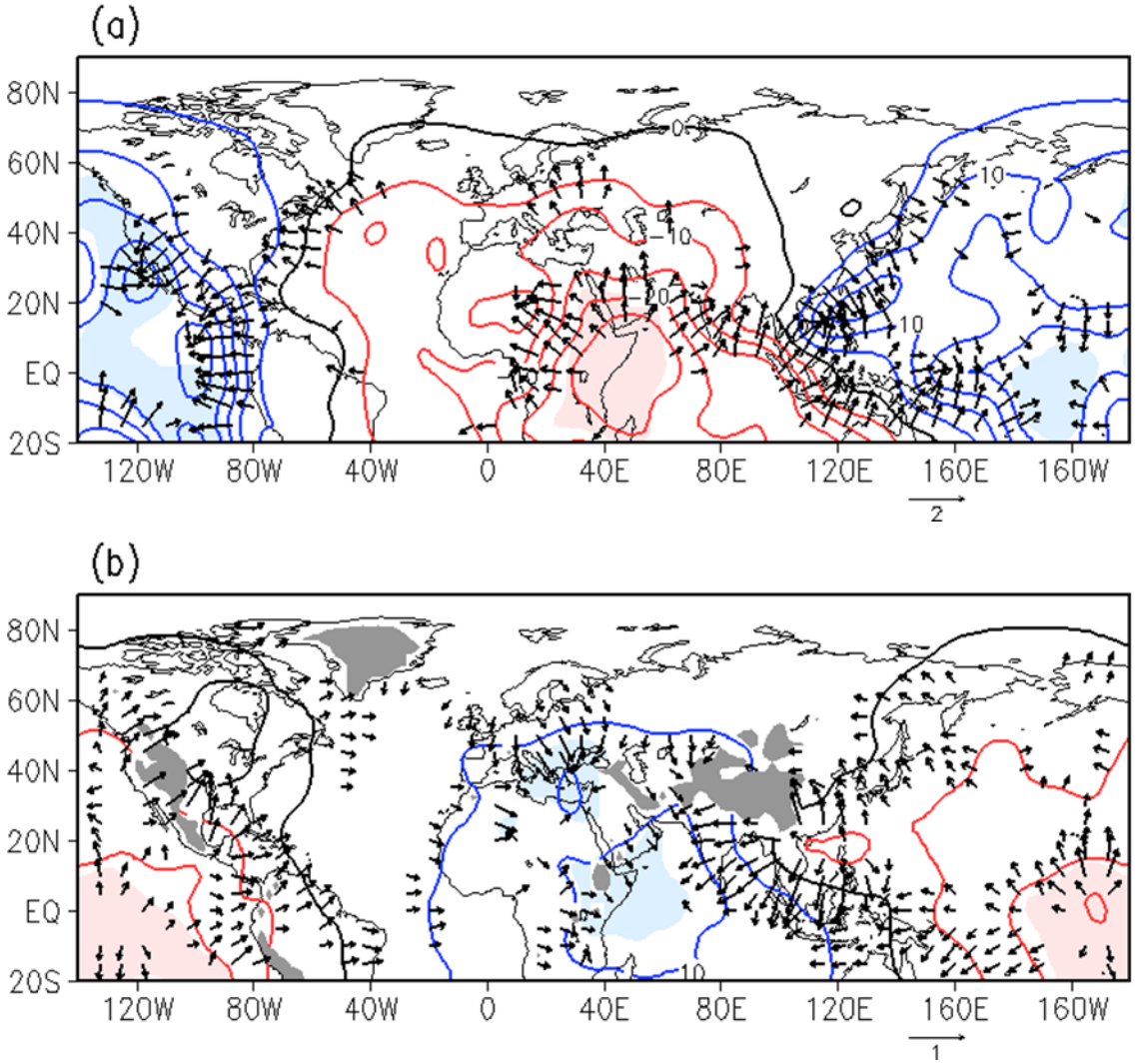

Fig. 4.4. As for Fig. 4.3, but for velocity potential at (a) 200 hPa and (b) 850 hPa averaged between day -12 and day -8. Contour represents velocity potential. Contour interval is 1×10^5 $m^2\ s^{-1}$. Shade represents statistically 95% confidence level. Arrows represent the divergence wind, and are plotted at grid points where the magnitude of the divergence wind is greater than (a) 0.5 and (b) 0.2 m s^{-1}.

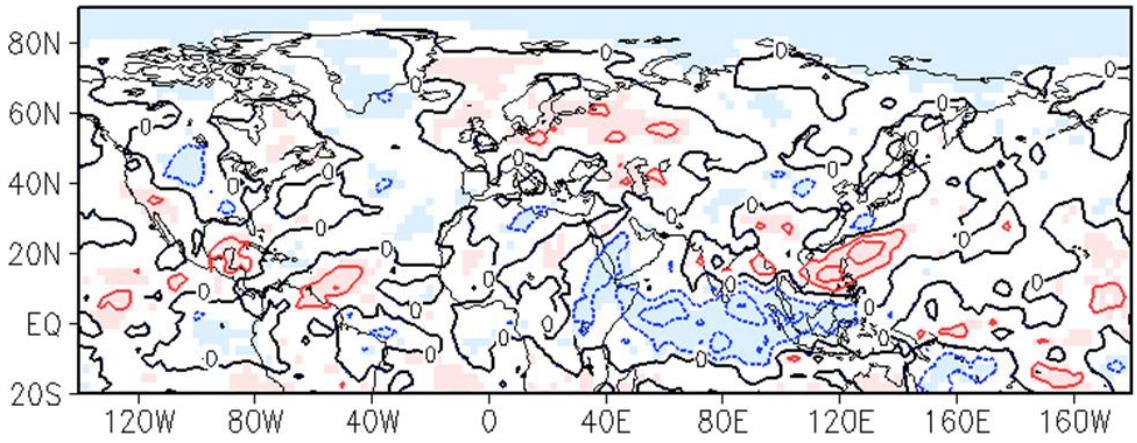

Fig. 4.5. As for Fig. 4.3, but for OLR averaged between day -12 ~ day -8. Contours represent OLR. Contour interval is 10 W m^{-2}. Shade represents statistically 95% confidence level.

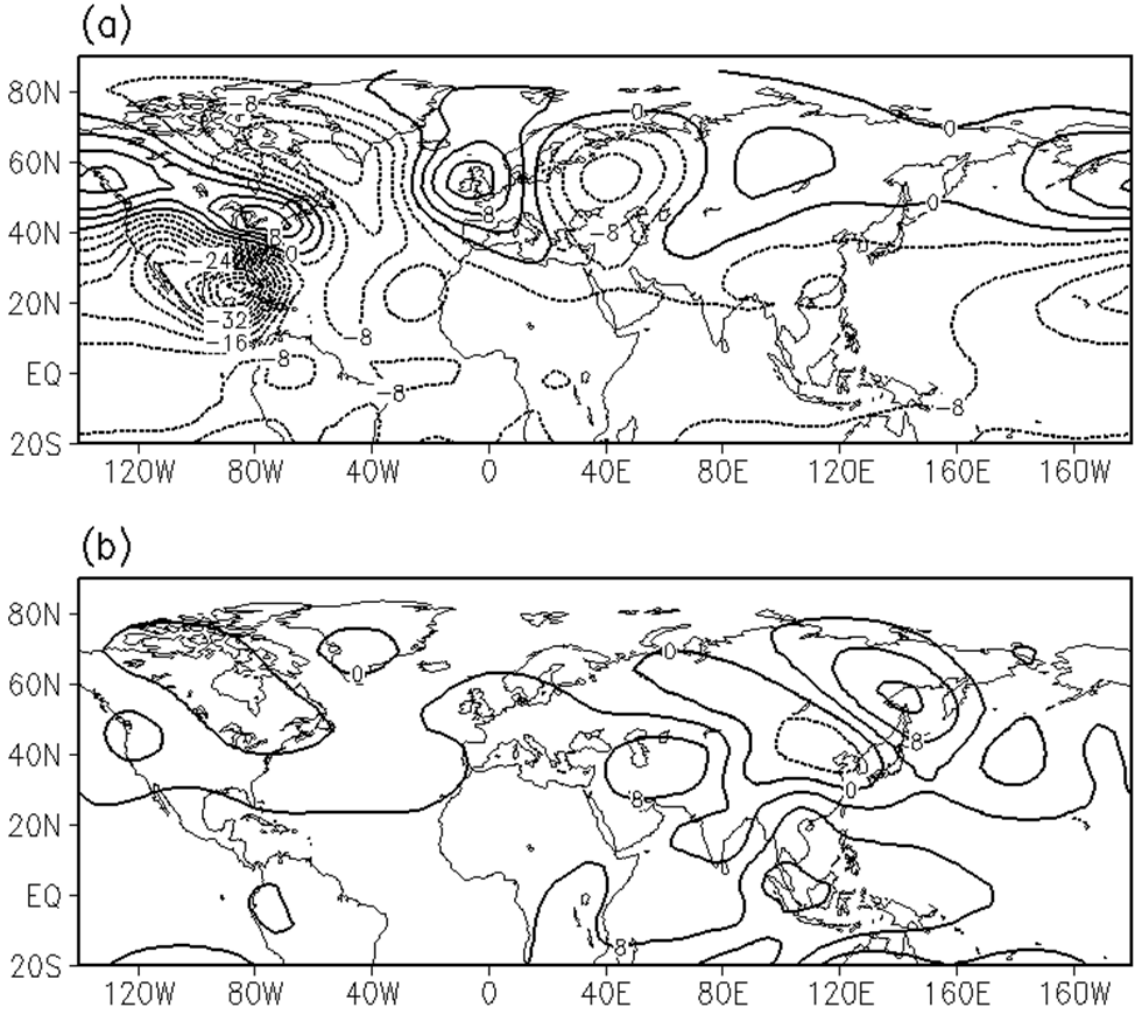

Fig. 4.6. Results from (a) the first, and (b) the second numerical LBM experiments showing the 30-day average from day 11 to day 40 of the integration. Contours represent the geopotential height at 200 hPa. Contour interval is 4 m.

5. General Summary

The present study aims to reveal the relation between the Asian summer monsoon and the middle latitudes on the intraseasonal scale. The present study proceeds with two viewpoints; the intraseasonal variation in early summer is targeted at. And the variation of geopotential height over the western Tibetan plateau is emphasized. Three subjects are worked on in three chapters one by one. Results of the present study are summarized as follows:

1) The mechanism of connection between the middle latitudes and the Asian monsoon through the anomaly over the western Tibetan plateau in early summer is found. It is particularly found the low-level westerly works as the Rossby wave guide and the low-level Rossby wave plays important role in connection between the Asian summer monsoon and the middle latitude in early summer.

2) Increase/decrease of precipitations over South and Southeast Asia is retained about a week after the marked anticyclonic/cyclonic anomaly over the western Tibetan plateau appears respectively. Before development of anomaly over the western Tibetan plateau the precipitation tend to vary due to the disturbance in the tropics. In the end the variation of precipitation persists for two weeks while the anomaly over the western Tibetan plateau develops and declines. At the same time variation of near-surface temperature persists too, which is caused by the cloud cover and precipitation.

3) The intraseasonal variation of geopotential height over the western Tibetan plateau is influenced by two factors. One is the wave train propagating from the northern Atlantic Ocean to the western Tibetan plateau via the western Russia. The other is variation of the convection over the northern Indian Ocean. The western Tibetan Plateau is the region where the effects in the tropics and middle latitudes tend to be concentrated, and it is thought to be an important connection between the Asian monsoon and middle latitudes. When the

large-scale disturbance in tropics like the MJO appears two factors tend to intensify the geopotential height anomaly simultaneously.

Acknowledgment

I would like to thank my supervisor Prof. Koji Yamazaki for his guidance on meteorology and suggestion on this thesis. I would like to thank Prof. Fumio Hasebe, Dr. Masaru Inatsu, and Dr. Tomonori Sato for useful comments. I also acknowledge lots of support from all members of Graduate School of Environmental Science, Hokkaido University.

References

Baldwin, M. P., D. B. Stephenson and I. T. Jolliffe, 2006: Spatial weighting and iterative projection methods for EOFs. 2009, J. Climate, 22, 234-243.

Barlow, M. and D. Salstein, 2006: Summertime influence of the Madden-Julian oscillation on daily rainfall over Mexico and Central America. Geophys. Res. Lett., 33, L21708, doi:10.1029/2006GL027738

Blake, D. W., T. K. Krishnamurti, S. V. Low-Nam, and J. S. Fein, 1983: Heat low over the Saudi Arabian desert during May 1979 (summer MONEX). Mon. Wea. Rev., 111, 1759–1775.

Gadgil, S., 1977: Orographic effects on the southwest monsoon: A review. Pure Appl. Geophys., 115, 1413–1430.

Holton, J. R., 2004: An Introduction to Dynamic Meteorology. 4th ed. Elsevier, 535 pp.

Hoskins, B. J., and T. Ambrizzi, 1993: Rossby wave propagation on a realistic longitudinally varying flow. J. Atmos. Sci., 50, 1661–1671.

—, I. Draghici, and H. C. Davies, 1978: A new look at the ω-equation. Quart. J. Roy. Meteor. Soc., 104, 31–38.

Joseph, P. V., and S. Sijikumar, 2004: Intraseasonal variability of the low-level jet stream of the Asian summer monsoon. J. Climate, 17, 1449–1458.

Kemball-Cook, S. and B. Wang, 2001: Equatorial waves and air-sea interaction in the boreal summer intraseasonal oscillation. J. Climate, 14, 2923-2942.

Liebmann, B., and C. A. Smith, 1996: Description of a complete (interpolated) outgoing longwave radiation dataset. Bull. Am. Meteorol. Soc., 77, 1275-1277.

Lorenz, D. J. and D. L. Hartmann, 2006: The effect of the MJO on the North America monsoon. J. Climate, 19, 333-343.

Madden R. A. and P. R. Julian, 1994: Observations of the 40-50-day tropical oscillation –A review. Mon. Wea. Rev., 122, 814-837.

Matthew. C. W., and H. H. Hendon, 2004: An all-season real-time multivariate MJO index: development of an index for monitioring and prediction. Mon. Wea. Rev., 132, 1917-1932.

Pai, D. S., J. Bhate, O. P. Sreejith and H. R. Hatwar, 2011; Impact of MJO on the intraseasonal variations of summer monsoon rainfall over India. Clim. Dyn., 36, 41-55.

Rodwell, M. J. and B. J. Hoskins, 1996: Monsoons and the dynamics of deserts. Q. J. R Meteorol. Soc., 122, 1385-1404.

Sardeshmukh, P., and B. J. Hoskins, 1988: The generation of global rotational flow by steady idealized tropical divergence. J. Atmos. Sci., 45, 1228-1251.

Smith, E. A., 1986: The structure of the Arabian heat low. Part II: Bulk tropospheric heat budget and implications. Mon. Wea. Rev., 114, 1084–1102.

Takaya K, H. Nakamura 2001: A formulation of a phase-independent wave-activity flux for stationary and migratory quasigeostrophic eddies on a zonally varying basic flow. J. Atmos. Sci., 58, 608-627.

Uppala, S. M., and Coauthors, 2005: The ERA-40 re-analysis. Q. J. R. Meteorol. Soc., 131, 2961-3012.

Wang, B., Q. Bao, B. Hoskins, G. Wu, and Y. Liu, 2008: Tibetan plateau warming and precipitation changes in East Asia. Geophys. Res. Lett., 35, L14702, doi:10.1029/2008GL034330.

Watanabe, M. and M. Kimoto, 2000: Atmosphere-ocean thermal coupling in the north Atlantic: A positive feedback. Q. J. R. Meteorol. Soc., 126, 3343-3369.

Webster, P. J., V. O. Magana, T. N. Palmar, J. Shukla, R. A. Tomas, M. Yanai, and T. Yasunari, 1998: Monsoon: processes, predictability, and the prospects for prediction. J. Geophys. Res., 103, 14,451-14,510

Yatagai, A., O. Arakawa, K. Kamiguchi, H. Kawamoto, M. I. Nodzu and A. Hamada, 2009: A 44-year daily gridded precipitation dataset for Asia based on a dense network of rain gauges. SOLA, 5, 137-140, doi:10.2151/sola.2009-035.

Zhang, A. and B. Wang, 2008: Global summer monsoon rainy seasons. Int. J. Climatol, 28, 1563-1578.

Zhang, Z., J. C. L. Chan and Y. Ding, 2004: Characteristics, evolution and mechanisms of the summer monsoon onset over Southeast Asia. Int. J. Climatol. 24. 1461-1482.